Situation-Aware Dithering for Dynamic Range Enhancement of a Mixed-Resolution ADC in Automotive Radar Receivers

Mohammed Aasim Shaikh, *Graduate Student Member, IEEE*, Geethu Joseph, *Senior Member, IEEE*, Ashish Pandharipande, *Senior Member, IEEE*, and Nitin Jonathan Myers, *Member, IEEE*

***Abstract*—Digital radars with low-resolution analog-to-digital converters (ADCs) have attracted attention as a solution to reducing the high digital processing complexity and power consumption at the receiver. Radars employing low-resolution ADCs, however, have a limited dynamic range, due to which high-radar cross section (RCS) targets mask low-RCS targets. The masking occurs because the quantized output is primarily determined by returns from high-RCS targets. To enhance the dynamic range of such radars, we propose to operate the ADC at a high resolution in the initial slow-time slot of each radar frame. The resulting high-resolution measurements are used together with the known Doppler statistics of dominant targets to construct a dither signal, which is used as a quantization threshold to acquire low-resolution ADC measurements in the subsequent slow-time slots. By incorporating situation awareness in the form of Doppler statistics, our dither signal can suppress returns from strong targets, effectively unmasking weak targets with low-resolution measurements. We analyze system performance in terms of the probability of detection and show that the proposed approach outperforms existing methods in enhancing the detection of weak targets. The simulations demonstrate that our method significantly improves target detection and reduces the normalized mean square error (NMSE) in the estimated radar channel over comparable benchmarks.**

***Index Terms*—Adaptive thresholding, digital low-resolution radar, environment-aware dithering, one-bit compressive sensing, situation-aware sensing.**

I. Introduction

THE automotive radars have become indispensable for enhancing the safety of advanced driver-assistance systems and fully autonomous driving systems [1]. Compared to sensors such as cameras and LiDARs, radars provide robust sensing capabilities, particularly under poor lighting conditions or adverse weather [2]. Although typical automotive radars employ analog frequency modulated continuous wave signals, there is an increasing interest in digital radar architectures, which offer higher flexibility in waveform design and signal processing [3], and superior interference rejection [4].

Digital radars quantize the analog signal obtained after downconverting the received return to the baseband [5]. A high sampling rate in digital radars results in a high-range resolution, and a high-precision quantizer results in low quantization noise. Achieving high-precision quantization requires high-resolution analog-to-digital converters (ADCs), which consume substantial power at high sampling rates. Furthermore, high-resolution wideband ADCs lead to an increased hardware complexity and cost of the radar and generate large data volumes that pose challenges in storage and processing [6]. The limitations of high-resolution wideband ADCs pose a challenge for automotive radars, where low-power consumption, fast real-time processing, and low cost are critical.

Considering the challenges with high-resolution wideband ADCs, recent work has studied the use of low-resolution ADCs in radars [7], [8], [9], [10], [11], [12], [13]. In particular, one-bit ADCs can be realized using a comparator that consumes significantly less power than its high-resolution counterparts. With one-bit ADCs, the amplitude of the received signal is reduced to just the polarity, i.e., positive or negative. Due to such coarse quantization, radars employing one-bit ADCs have a limited dynamic range, which impairs the detection of low-radar cross section (RCS) targets in the presence of stronger reflections [14], [15]. This is because the quantized output of the ADC is primarily determined by the stronger reflections from high-RCS targets, which makes it hard to detect reflections from low-RCS targets such as pedestrians. The reduced dynamic range with low-resolution radars, such as one-bit radars, poses a risk in safety-critical automotive applications.

A recent study has investigated methods to improve detection with low-resolution radars by introducing time-varying thresholds at the ADC prior to quantization [16], [17], [18]. This process is called dithering, and the dither signal comprises time-varying thresholds. For example, Shang et al. [17] employ a random dither signal, whose entries are uniformly distributed in $[-1, 1]$. Although such a dither signal can enhance the radar's dynamic range in specific scenarios, it does not adapt to the scene being scanned. In [18], a dither signal is generated using the mean and covariance information of reflection coefficients and Doppler shifts for the target of interest and clutter. This article resolves the uncertainty

Received 17 May 2025; revised 1 August 2025; accepted 2 October 2025. Date of publication 10 October 2025; date of current version 24 November 2025. This work was supported in part by NXP Semiconductors and in part by Netherlands Enterprise Agency under Grant PPS2207. *(Corresponding author: Nitin Jonathan Myers.)*

Mohammed Aasim Shaikh and Nitin Jonathan Myers are with the Delft Center for Systems and Control, Delft University of Technology, 2628 Delft, The Netherlands (e-mail: M.A.Shaikh@tudelft.nl; n.j.myers@tudelft.nl).

Geethu Joseph is with the Department of Microelectronics, Delft University of Technology, 2628 Delft, The Netherlands (e-mail: g.joseph@tudelft.nl).

Ashish Pandharipande is with NXP Semiconductors, 5656 Eindhoven, The Netherlands (e-mail: ashish.pandharipande@nxp.com).

Digital Object Identifier 10.1109/TRS.2025.3620087

in high-RCS reflection coefficients by acquiring a few high-resolution samples, allowing the dither signal to be tailored to the radar channel realization. Similar to [18] and [19] mitigate clutter in one-bit radars by designing the dither signal using clutter statistics, while [20] mitigates radio frequency interference in one-bit radar by estimating the interference parameters, assuming the interference to be significantly stronger than the radar echo signal. In [21], the static quantization thresholds are optimized by minimizing the Cramér–Rao lower bound (CRLB) for target localization in a wireless sensor network. Applying this approach in our framework, however, requires solving an optimization problem to determine the thresholds for every slow-time slot, making it less suitable for real-time dithering. In [22], the quantization thresholds are recentered based on coarse signal estimates; however, these remain fixed across pulses. In contrast, our method generates time-varying, Doppler-aware dither thresholds that adaptively cancel high-RCS targets, enhancing the detection of low-RCS targets. Finally, the dithering methods in [23], [24], and [25] are based on filter design and numerical optimization, due to which real-time dither signal generation is challenging. Our goal is to develop a technique that adapts to the environment being scanned, while aiding fast real-time generation of the dither signal.

Prior work has studied sparse recovery-based parameter estimation with multiple-input multiple-output (MIMO) radars employing few-bit ADCs [15], [26]. When the targets are widely spaced, these systems achieve similar performance as radars with high-precision ADCs [26]. The performance with few-bit ADC radars, however, deteriorates when the targets are closely spaced or when the RCS of the targets is substantially different [15]. Mixed-ADC MIMO radars, where a subset of antennas is equipped with high-precision ADCs while the rest employ one-bit ADCs, were investigated in [27] and [28]. To address the dynamic range issue with one-bit ADCs, Shang et al. [27] employed a dithering signal, whose entries are first drawn from $[-1, 1]$ and then scaled by the average received signal amplitude. The mixed-resolution multi-output architectures in [27] and [28] fix the ADC resolution over time. In this article, we consider a single-output receiver whose ADC resolution can be dynamically adapted over the slow-time dimension.

Our framework sets the ADC resolution to a high value (e.g., 16 bits) in the first slow-time slot and employs a low resolution (e.g., 1 bit) in the subsequent slots within the coherent processing interval (CPI). This slow-time resolution adaptation can be achieved by dynamically tuning quantization thresholds [29], adjusting the oversampling rate in a Σ-Δ ADC [30], or introducing resolution switches within a successive approximation register ADC [31]. These methods enable dynamic resolution adaptation within the same ADC hardware.

The ADC architecture considered in this article differs from the unlimited one-bit (UNO) design [32], which is based on unlimited sampling [33] for signal recovery from folded (modulo) measurements. The UNO ADCs operate in an oversampling mode throughout the entire CPI, leading to an increased data throughput and computational complexity. In contrast, our method (with Σ-Δ ADCs) requires oversampling only in the initial slow-time slot. The UNO addresses quantization saturation by allowing signals that exceed conventional ADC ranges to wrap around rather than clip, thereby supporting high-dynamic range acquisition. The reconstruction accuracy degrades with the input dynamic range of the signal because the number of modulo operations increases. Our situation-aware dithering technique can address the dynamic range issue with [33], by performing analog cancellation prior to ADC quantization. Integrating UNO ADCs within our framework is beyond the scope of this article and would be an interesting direction for future work.

In our system, the initial high-resolution measurements are used to estimate the range and RCS of strong reflectors. These estimates, along with the Doppler statistics representing environmental context, are then used to construct a situation-aware dither signal. This dither is designed to suppress the influence of high-RCS targets on the quantized measurements, mitigating the masking effect and thereby enhancing the detectability of low-RCS targets.

Our key contributions are summarized as follows.

1) We propose a situation-aware dithering technique that uses a few high-resolution radar measurements and Doppler statistics to generate a dither signal. The generated dither signal is used as a dynamic threshold in acquiring low-resolution radar measurements.
2) We develop a three-stage procedure for radar channel estimation from mixed-resolution measurements. The first stage determines the range and RCS of dominant targets to generate the dither signal. The second stage estimates the radar channel from low-resolution measurements acquired with the dither signal. Finally, the third stage compensates for the scaling ambiguity in the estimated radar channel.
3) We derive the probability of detection as a function of the dither signal, by considering a two-target scenario. Using the derived probability, we numerically show that the designed dither signal achieves better detection than existing dithering methods.
4) We show by simulations that our approach enhances the detection of low-RCS targets and reduces the normalized mean square error (NMSE) of the estimated radar channel over comparable benchmarks.

In this article, we assume that the maximum number of targets in any range bin is one, e.g., it is not possible to observe targets at 10 m with two different Dopplers. In practice, this assumption can be justified when the radar has sufficient range resolution and can isolate returns from each direction by employing beamforming. We also consider the extreme case of 1-bit for low-resolution quantization. Our framework, however, can be directly applied to radars using few-bit ADCs by using the appropriate likelihood function in our objective.

Notation: Scalars (e.g., x) are denoted in italic letters. Deterministic vectors (e.g., $\boldsymbol{x}$) are represented in italic bold letters, while matrices (e.g., $\boldsymbol{X}$) are denoted in italic bold capital letters. Random variables (e.g., x) are represented in normal letters, whereas random vectors (e.g., $\mathbf{x}$) and random matrices (e.g., $\mathbf{X}$) are denoted in bold normal and bold capital normal letters, respectively. The probability of an event is denoted by $\mathcal{P}(\cdot)$. The Hadamard product is denoted by $\odot$ and

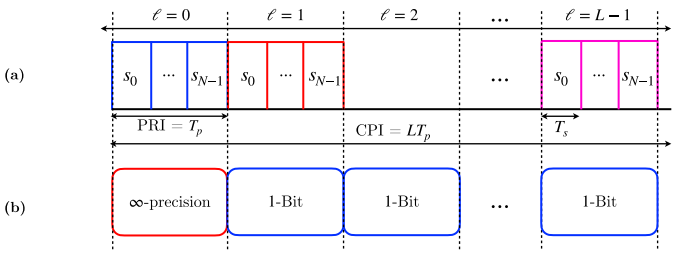

Fig. 1. Transmit signal and resolution at the receiver ADC. We consider a digital radar transmitter that periodically transmits a sequence $\boldsymbol{s}$ every PRI. (a) Sketch of this signal. (b) Receiver uses an ADC whose resolution can be adapted in slow time. In this article, the ADC's resolution is set high only during the first slow-time slot of each CPI.

the Kronecker product by $\otimes$. The complex conjugate operation is denoted by $(\cdot)^*$. $(\cdot)^{\mathrm{T}}$ indicates the transpose, while $(\cdot)^{\mathrm{H}}$ represents the complex conjugate transpose (Hermitian).

For a vector $\boldsymbol{x}$ and matrix $\boldsymbol{X}$, their real-valued representations, denoted by $\tilde{(\cdot)}$, respectively, are defined as

$$\tilde{\boldsymbol{x}} = \begin{bmatrix} \Re(\boldsymbol{x}) \\ \Im(\boldsymbol{x}) \end{bmatrix}, \quad \text{and} \quad \tilde{\boldsymbol{X}} = \begin{bmatrix} \Re(\boldsymbol{X}) & -\Im(\boldsymbol{X}) \\ \Im(\boldsymbol{X}) & \Re(\boldsymbol{X}) \end{bmatrix}$$

where $\Re(\cdot)$ returns the real part and $\Im(\cdot)$ the imaginary part.

II. System Model and Sparse Channel Recovery

We consider a digital radar system in a single-input single-output configuration. The transmitted signal, shown in Fig. 1(a), is constructed by periodically repeating the digital sequence $\boldsymbol{s} = \left[s(0)\ s(1)\ \cdots\ s(N-1)\right]^{\mathrm{T}}$, where N is the sequence length, and $(\cdot)^{\mathrm{T}}$ denotes the transpose. We define T_s as the chip duration and $T_p = NT_s$ as the pulse repetition interval (PRI). We use L to denote the slow-time slots within each CPI. These slots are indexed by $\ell \in \{0, 1, 2, \ldots, L-1\}$. As shown in Fig. 1(b), our receiver uses an infinite resolution at the ADC in the first slow-time slot ($\ell = 0$) and 1-bit resolution in the remaining $L-1$ slots ($1 \le \ell \le L-1$).

In this section, we discuss the system model for 1-bit measurements acquired using a generic dither signal and the associated radar channel estimation algorithm. In Section III, we explain how to use the high-resolution measurements from the first slot to construct our dither signal and update the radar channel estimate.

A. Measurement Model for One-Bit ADCs With Dithering

For the signaling structure in Fig. 1(a), the baseband representation of the transmitted signal is

$$s_{\mathrm{TX}}(t) = \sum_{\ell=-\infty}^{\infty} \sum_{n=0}^{N-1} s(n)\, p\left(t - nT_s - \ell T_p\right)$$

where $p(t)$ is a rectangular pulse of duration T_s (unity for $0 \le t \le T_s$ and zero otherwise). We partition the range and Doppler domains into $N_r (N_r \le N)$ and N_d discrete bins, with bins indices denoted by n_r and n_d, respectively. The received signal is then

$$z(t) = \sum_{n_r=1}^{N_r} \sum_{n_d=1}^{N_d} \gamma_{n_r n_d} s_{\mathrm{TX}}\left(t - \tau_{n_r}\right) e^{j2\pi f_{n_d} t} + e(t) \tag{1}$$

where $\tau_{n_r} = n_r T_s$ denotes the time delay, f_{n_d} denotes the Doppler shift, $\gamma_{n_r n_d}$ denotes the reflection coefficient of the target in the (n_r, n_d)th bin, and $e(t)$ is the additive noise.

We derive the discrete-time representation of $z(t)$ in (1) over L slow-time slots. Such a representation models the unquantized signal, which will be later dithered and quantized. We ignore the phase variation due to Doppler within a PRI. Under this assumption, the received baseband signal in (1) for the ℓth slow-time slot is

$$z_\ell(t) = \sum_{n_r, n_d} \sum_{n=0}^{N-1} \gamma_{n_r n_d} s\left((n + n_r) \bmod N\right) \times p\left(t - (n_r + n) T_s\right) e^{j2\pi \nu_{n_d} \ell} + e(t)$$

where $\nu_{n_d} = f_{n_d} T_p$, and $(n+n_r) \bmod N$ are the remainder when $(n + n_r)$ is divided by N. The discrete-time representation of $z_\ell(t)$ at the N time instances in $\{\ell T_p, \ldots, \ell T_p + (N-1)T_s\}$ is then

$$\boldsymbol{z}_\ell = \boldsymbol{S}\boldsymbol{\Gamma}\boldsymbol{a}_\ell + \boldsymbol{e}_\ell$$

where $\boldsymbol{\Gamma}$ is the reflection coefficient matrix of the scene, and $\boldsymbol{a}_\ell$ is the steering vector, defined as

$$\boldsymbol{\Gamma} = \begin{bmatrix} \gamma_{11} & \gamma_{12} & \cdots & \gamma_{1N_d} \\ \gamma_{21} & \gamma_{22} & \cdots & \gamma_{2N_d} \\ \vdots & \vdots & \ddots & \vdots \\ \gamma_{N_r 1} & \gamma_{N_r 2} & \cdots & \gamma_{N_r N_d} \end{bmatrix} \in \mathbb{C}^{N_r \times N_d}$$

$$\boldsymbol{a}_\ell = \left[e^{j2\pi \nu_1 \ell}, e^{j2\pi \nu_2 \ell}, \cdots, e^{j2\pi \nu_{N_d} \ell}\right]^{\mathrm{T}}$$

$$\boldsymbol{S} = \begin{bmatrix} s(0) & s(N-1) & \cdots & s(N-N_r+1) \\ s(1) & s(0) & \cdots & s(N-N_r+2) \\ \vdots & \vdots & \ddots & \vdots \\ s(N-1) & s(N-2) & \cdots & s(N-N_r) \end{bmatrix}. \tag{2}$$

The goal of this article is to estimate $\boldsymbol{\Gamma}$, the range-Doppler radar channel matrix, from its mixed-resolution measurements.

We observe, from the ADC resolutions in Fig. 1, that the signal received in the first slow-time slot is unquantized, i.e., the receiver acquires $\boldsymbol{z}_0$. The remaining $L-1$ vectors corresponding to the subsequent slow-time slots, i.e., $\{\boldsymbol{z}_\ell\}_{\ell=1}^{L-1}$, are quantized to one-bit. To construct the one-bit measurement model, we first write the collection of unquantized vectors as

$$\boldsymbol{Z} = [\boldsymbol{z}_1, \boldsymbol{z}_2, \ldots, \boldsymbol{z}_{L-1}] = \boldsymbol{S}\boldsymbol{\Gamma}\boldsymbol{A} + \boldsymbol{E}$$

where $\boldsymbol{A} = [\boldsymbol{a}_1, \boldsymbol{a}_2, \ldots, \boldsymbol{a}_{L-1}]$ is the Vandermonde matrix and $\boldsymbol{E} = [\boldsymbol{e}_1, \boldsymbol{e}_2, \ldots, \boldsymbol{e}_{L-1}]$ is the noise matrix. By vectorizing $\boldsymbol{\Gamma}$ as $\boldsymbol{\gamma} = \mathrm{vec}(\boldsymbol{\Gamma})$, and similarly defining $\boldsymbol{z} = \mathrm{vec}(\boldsymbol{Z})$ and $\boldsymbol{e} = \mathrm{vec}(\boldsymbol{E})$, we obtain

$$\boldsymbol{z} = \boldsymbol{B}\boldsymbol{\gamma} + \boldsymbol{e}, \quad \boldsymbol{B} = \boldsymbol{A}^{\mathrm{T}} \otimes \boldsymbol{S}. \tag{3}$$

The vector $\boldsymbol{z}$ has $N(L-1)$ entries as it models the unquantized discrete-time signal for $L-1$ slow-time slots. This vector is first dithered, equivalently subtracted, using a discrete-time representation of a known analog dither signal $\boldsymbol{q}(t)$. We denote $\boldsymbol{q} = \boldsymbol{q}_\Re + j\boldsymbol{q}_\Im$ as the discrete-time version of $\boldsymbol{q}(t)$ and write the dithered signal as $\boldsymbol{z} - \boldsymbol{q}$. The dithered signal is finally quantized using a one-bit ADC to output

$$\begin{cases} \boldsymbol{y}_\Re = \mathrm{sign}\left(\Re[\boldsymbol{z}] - \boldsymbol{q}_\Re\right) \\ \boldsymbol{y}_\Im = \mathrm{sign}\left(\Im[\boldsymbol{z}] - \boldsymbol{q}_\Im\right) \end{cases} \tag{4}$$

where sign(·) denotes the sign function which is −1 for negative arguments and + 1 otherwise. The complex measurement vector $\boldsymbol{y}$ can then be written as

$$\boldsymbol{y} = \boldsymbol{y}_{\Re} + j\boldsymbol{y}_{\Im}.$$

In automotive radar applications, the range-Doppler radar channel $\boldsymbol{\Gamma}$ is sparse. The sparse structure is due to several unoccupied cells in a high-dimensional range-Doppler grid and the high scattering at typical carrier frequencies used in automotive radars. Such a structure enables the use of compressed sensing (CS)-based techniques, which can exploit sparse priors in radar channel reconstruction.

B. One-Bit Sparse Recovery With Dithered Measurements

We discuss how $\boldsymbol{\Gamma}$, equivalently its vector version $\boldsymbol{\gamma}$, can be estimated from the one-bit quantized measurements $\boldsymbol{y}$ and the known dither signal $\boldsymbol{q}$. To this end, we employ the one-bit CS method based on log-sum penalty minimization [17]. While alternative one-bit CS methods could also be applied, we would like to emphasize that the focus of this article is not on sparse recovery itself, but on designing a dither signal and estimating radar channels from mixed-resolution measurements. Therefore, the one-bit CS algorithm, such as the approach in [17], is just one component in our channel estimation method.

The one-bit CS technique in [17] enforces sparsity by minimizing the log-sum penalty discussed in [34]. Assume that $\mathbf{e}$ is a independent and identically distributed (i.i.d.) circularly symmetric complex Gaussian noise vector with zero mean and unknown variance σ^2. Specifically, the real and imaginary parts of $\mathrm{e}(m)$ are independently distributed as $\Re[\mathrm{e}(m)] \sim \mathcal{N}(0, \sigma^2/2)$ and $\Im[\mathrm{e}(m)] \sim \mathcal{N}(0, \sigma^2/2)$, respectively. Under this assumption, the negative log-likelihood of the signed measurement vector is [16], [35], [36], and [37]

$$\mathcal{L}(\boldsymbol{\gamma}, \sigma) = -\sum_{m=1}^{NL-N} \log \Phi\left(y_{\Re}(m) \frac{\Re\left[\boldsymbol{b}_m^{\mathrm{T}}\boldsymbol{\gamma}\right] - \boldsymbol{q}_{\Re}(m)}{\sqrt{\sigma^2/2}} \right) - \sum_{m=1}^{NL-N} \log \Phi\left(y_{\Im}(m) \frac{\Im\left[\boldsymbol{b}_m^{\mathrm{T}}\boldsymbol{\gamma}\right] - \boldsymbol{q}_{\Im}(m)}{\sqrt{\sigma^2/2}} \right)$$

where $\Phi(x)$ is the cumulative distribution function of the standard Gaussian distribution, and $\boldsymbol{b}_m^{\mathrm{T}}$ denotes the mth row of the matrix $\boldsymbol{B}$. To express $\mathcal{L}(\boldsymbol{\gamma}, \sigma)$ in compact form, we define $\eta = \sqrt{2}/\sigma$, $\boldsymbol{\beta} = \eta\boldsymbol{\gamma}$ and write

$$\mathcal{L}(\boldsymbol{\beta}, \eta) = -\sum_{m=1}^{NL-N} \log \Phi\left(y_{\Re}(m) \left(\Re\left[\boldsymbol{b}_m^{\mathrm{T}}\boldsymbol{\beta}\right] - \eta \boldsymbol{q}_{\Re}(m) \right) \right) - \sum_{m=1}^{NL-N} \log \Phi\left(y_{\Im}(m) \left(\Im\left[\boldsymbol{b}_m^{\mathrm{T}}\boldsymbol{\beta}\right] - \eta \boldsymbol{q}_{\Im}(m) \right) \right).$$

Note that estimating $\boldsymbol{\beta}$ is equivalent to estimating the radar channel vector $\boldsymbol{\gamma} = \boldsymbol{\beta}/\eta$. The approach in [17] minimizes the negative log-likelihood $\mathcal{L}(\boldsymbol{\beta}, \eta)$ while enforcing a sparse prior on $\boldsymbol{\beta}$. This is achieved by adding a log-sum penalty as a regularization term and minimizing the cost

$$G(\boldsymbol{\beta}, \eta) = \mathcal{L}(\boldsymbol{\beta}, \eta) + \alpha \sum_{k=1}^{N_r N_d} \log\left(|\beta_k|^2 + \epsilon \right).$$

Here, $\alpha > 0$ controls the balance between data fidelity and sparsity, and $\epsilon > 0$ ensures numerical stability.

The cost $G(\boldsymbol{\beta}, \eta)$ is nonconvex, and the approach in [17] derives convex majorization functions for both $\mathcal{L}(\boldsymbol{\beta}, \eta)$ and the log-sum penalty term. The estimate of $\tilde{\boldsymbol{\beta}}$, the real-valued representation of $\boldsymbol{\beta}$, at the $(t+1)$th iteration is obtained by minimizing the majorized objective function [17], i.e.,

$$\hat{\tilde{\boldsymbol{\beta}}}^{t+1} = \left(\tilde{\boldsymbol{B}}^{\mathrm{T}}\tilde{\boldsymbol{B}} + 2\alpha\tilde{\boldsymbol{D}}^{t} \right)^{-1} \left(\tilde{\boldsymbol{B}}^{\mathrm{T}} \left(\tilde{\boldsymbol{g}}^{t} + \eta\tilde{\boldsymbol{q}} \right) \right). \tag{5}$$

The vector $\tilde{\boldsymbol{g}}^{t}$ in (5) is [17]

$$\tilde{\boldsymbol{g}}^{t} = \begin{bmatrix} y_{\Re}(1)\, u_{\Re}^{t}(1), \ldots, y_{\Re}(M)\, u_{\Re}^{t}(M) \\ y_{\Im}(1)\, u_{\Im}^{t}(1), \ldots, y_{\Im}(M)\, u_{\Im}^{t}(M) \end{bmatrix}^{\mathrm{T}}$$

where we define

$$u_{\Re}(m) = x_{\Re}^{t}(m) + \psi\left(x_{\Re}^{t}(m) \right) / \Phi\left(x_{\Re}^{t}(m) \right). \tag{6}$$

Here, $\psi(\cdot)$ is the probability density function (pdf) of the standard normal distribution and

$$x_{\Re}^{t}(m) = y_{\Re}(m) \left(\Re\left[\boldsymbol{b}_m^{\mathrm{T}}\boldsymbol{\beta}^{t}\right] - \eta \boldsymbol{q}_{\Re}(m) \right). \tag{7}$$

Similarly, $u_{\Im}(m)$ and $x_{\Im}^{t}(m)$ are found by replacing $\Re$ by $\Im$ in (6) and (7). Finally, $\tilde{\boldsymbol{D}}^{t} = \mathrm{diag}([\boldsymbol{d}_t; \boldsymbol{d}_t])$ with

$$\boldsymbol{d}_t = \left[\frac{1}{\left|\hat{\beta}(1)\right|^2 + \epsilon}, \ldots, \frac{1}{\left|\hat{\beta}(N_r N_d)\right|^2 + \epsilon} \right]^{\mathrm{T}}.$$

The computational complexity of the update in (5) is dominated by the inverse operation over $\tilde{\boldsymbol{B}}^{\mathrm{T}}\tilde{\boldsymbol{B}} + 2\alpha\tilde{\boldsymbol{D}}^{t}$. In Section III-D, we discuss an efficient choice of the transmit sequence and the range-Doppler grid sizes that make $\tilde{\boldsymbol{B}}^{\mathrm{T}}\tilde{\boldsymbol{B}} + 2\alpha\tilde{\boldsymbol{D}}^{t}$ diagonal, thereby achieving a low-complexity implementation.

III. Situation-Aware Dithering and Radar Channel Estimation From Mixed-Resolution Measurements

In this section, we propose our receiver architecture to construct a situation-aware dither signal and perform channel estimation. Our dither signal alleviates the masking effect induced by high-RCS targets on low-RCS targets in one-bit sparse recovery. As shown in Fig. 2, our architecture combines Doppler statistics of high-RCS targets with their range and RCS estimates, which are obtained from the first slow-time interval ($\ell = 0$), to generate dither signals for subsequent slow-time slots. Our dither signals, which "predict" future returns from high-RCS targets, are subtracted from the received analog returns for $1 \le \ell \le L-1$.

We build toward our receiver architecture in Section III-C by first considering a setting with one high-RCS and one low-RCS target. While case 1 in Section III-A assumes that the Doppler of the high-RCS target is perfectly known, case 2 in Section III-B assumes that only the probability distribution of the high-RCS target's Doppler is known. In both cases, we describe our receiver architecture, which includes dither signal construction and the range-Doppler channel estimation. Finally, in Section III-C, we extend our receiver architecture to a general scenario with multiple targets, each associated with its own known Doppler distribution.

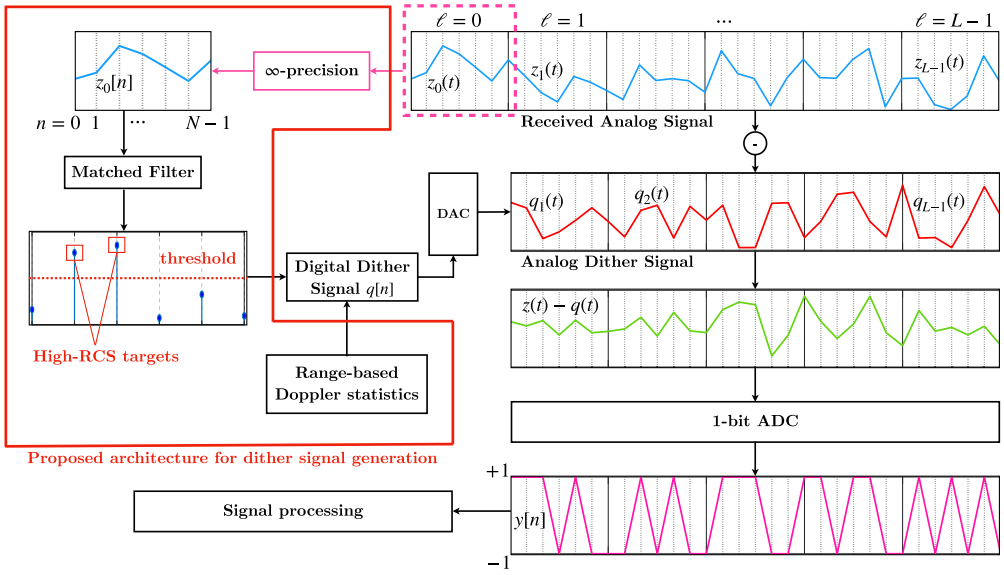

Fig. 2. Matched filter is applied over the high-resolution measurements from the first slow-time slot to detect high-RCS targets. The range and RCS estimates of these targets, together with the Doppler statistics, are used to generate a dither signal. One-bit measurements are acquired in the subsequent slow-time slots using the generated dither signal.

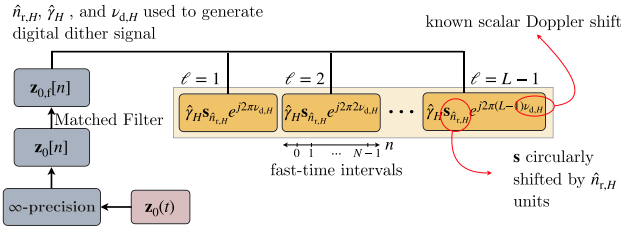

Fig. 3. Our dither signal generation method when the Doppler of a high-RCS target is perfectly known. The use of our dither signal attenuates the effective returns from the high-RCS target for slow-time slots $\ell \geq 1$, unmasking the low-RCS targets.

A. Case 1: Receiver Architecture for Perfectly Known Doppler (Single High-RCS and Single Low-RCS Target)

We assume that the high-RCS target's Doppler is known a priori and denote this Doppler as $\nu_{d,H}$. By using this Doppler information, future returns from the high-RCS target within a CPI can be predicted. The prediction, however, requires an estimate of the range and the RCS of the high-RCS target. To estimate these quantities, we propose to use high resolution at the ADC in the first slow-time slot, as shown in Fig. 1(b). The high-precision measurements from this slot ($\ell = 0$), denoted as $z_0[n]$, are processed using a matched filter to determine the range and RCS of the high-RCS target. The matched filtered signal $z_{0,f}[n]$ is given by

$$z_{0,f}[n] = \sum_{k=0}^{N-1} z_0[k]\, s^*[n-k]. \tag{8}$$

The amplitude and index of $z_{0,f}[n]$ at its maximum magnitude, $|z_{0,f}[n]|$, provide estimates for the RCS and range of the high-RCS target. In scenarios with multiple high-RCS targets, a user-defined threshold, μ, can be employed to identify such targets. The high-RCS targets can be identified from the indices where the matched filter magnitudes exceed μ, i.e., $\{n : |z_{0,f}[n]| > \mu\}$. In the single high-RCS target case, there is only one such index. We denote $\hat{\gamma}_H$ as the estimated RCS and $\hat{n}_{r,H}$ as the estimated range bin associated with the high-RCS target. As the high-RCS target's Doppler is known to be $\nu_{d,H}$, the return expected from this target in a subsequent slow-time slot ℓ is given by $\hat{\gamma}_H \boldsymbol{s}_{\hat{n}_{r,H}}[n] e^{j2\pi\nu_{d,H}\ell}$. Here, $\boldsymbol{s}_{\hat{n}_{r,H}}$ denotes a circularly shifted version of the transmit sequence $\boldsymbol{s}$ by $\hat{n}_{r,H}$ units. In this case, we set the dither signal to the expected return from the high-RCS target, i.e.,

$$\boldsymbol{q}_\ell[n] = \hat{\gamma}_H \boldsymbol{s}_{\hat{n}_{r,H}}[n]\, e^{j2\pi\nu_{d,H}\ell} \quad \forall\ \ell \geq 1. \tag{9}$$

Our dithering technique for this case is shown in Fig. 3. The analog version of the dither signal in (9) is subtracted from the unquantized signal in the subsequent slow-time slots as shown in Fig. 2. This dithering is performed to aid in detecting low-RCS targets from the quantized one-bit measurements.

The receiver uses the dither signal in (9) to acquire the one-bit measurement vector $\boldsymbol{y}$ using (4). The dither vector $\boldsymbol{q}$ corresponding to (9) is

$$\boldsymbol{q} = \left[\boldsymbol{q}_1, \boldsymbol{q}_2, \ldots, \boldsymbol{q}_{L-1}\right]. \tag{10}$$

The measurements acquired using $\boldsymbol{q}$ are used to estimate the range-Doppler radar channel using (5). The estimate obtained, however, is coarse due to two reasons. First, the effective return from the high-RCS target is significantly attenuated due to dithering, resulting in a reduced reflection coefficient for this target in the channel estimate. This reduction is key to observing the low-RCS target in the channel estimate from one-bit measurements. Second, one-bit sparse recovery can estimate the radar channel only up to a positive scale factor. This is because $\text{sign}(az) = \text{sign}(z)\ \forall\ a > 0$. To address the high-RCS target attenuation with dithering and the scaling ambiguity in one-bit sparse recovery, we propose a two-step approach to separately determine the reflection coefficients of high-RCS and low-RCS targets. Although we discuss our two-step approach for the single high-RCS and single

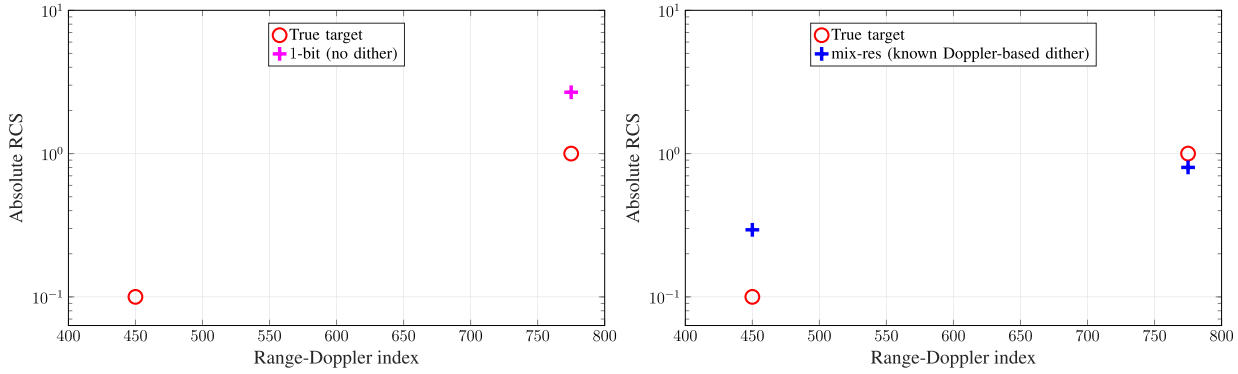

Fig. 4. Channel estimates in a scenario with a low-RCS target ($|\gamma| = 0.1$) and a high-RCS target ($|\gamma| = 1$) whose Doppler is perfectly known. Our method uses Doppler information and high-resolution samples from the first slow-time slot to generate a dither signal. This dither signal enables low-RCS target detection, unlike a conventional one-bit receiver with zero dither. (a) Conventional one-bit receiver ($q = 0$). (b) Proposed mixed-resolution receiver for known Doppler.

low-RCS scenario, the same procedure applies to the scenarios in Sections III-B and III-C.

1) Channel Estimation With Mixed-Resolution Measurements: Let $\hat{\boldsymbol{\beta}}_{\text{ob}} \in \mathbb{C}^{N_r N_d}$ be the sparse vector estimated from the one-bit measurements using (5). Its range-Doppler matrix representation, denoted by $\hat{\boldsymbol{X}}_{\text{ob}} \in \mathbb{C}^{N_r \times N_d}$, is obtained by reshaping $\hat{\boldsymbol{\beta}}_{\text{ob}}$ such that $\hat{\boldsymbol{\beta}}_{\text{ob}} = \text{vec}(\hat{\boldsymbol{X}}_{\text{ob}})$. Given our assumption that the maximum number of targets in any range bin is one, some false alarms in $\hat{\boldsymbol{X}}_{\text{ob}}$ can be eliminated. This is done by retaining only the strongest coefficient in each row (range-bin) of $\hat{\boldsymbol{X}}_{\text{ob}}$. To mask the false alarms, we define a binary matrix $\mathbf{M}_{\text{ob}} \in \{0,1\}^{N_r \times N_d}$ as

$$\mathbf{M}_{\text{ob}}[i,j] = \begin{cases} 1, & \text{if } j = \underset{k}{\text{argmax}} \, |\hat{\boldsymbol{X}}_{\text{ob}}[i,k]| \\ 0, & \text{otherwise.} \end{cases} \tag{11}$$

The masked channel estimate with no more than two targets in any range bin is

$$\hat{\boldsymbol{X}}_{\text{ob, filt}} = \mathbf{M}_{\text{ob}} \odot \hat{\boldsymbol{X}}_{\text{ob}}. \tag{12}$$

The estimate $\hat{\boldsymbol{X}}_{\text{ob, filt}}$ has range, Doppler, and RCS information of the targets identified with one-bit sparse recovery using (5).

We discuss how we estimate the radar channel corresponding to high-RCS targets using $\mathbf{M}_{\text{ob}}$ and the matched filter output in (8) at $\ell = 0$. As the high-RCS target is attenuated in $\hat{\boldsymbol{X}}_{\text{ob}}$ due to dithering, we use the matched filter output to estimate its range and RCS. The Doppler associated with the high-RCS target in range bin $\hat{n}_{r_h}$ is determined from $\mathbf{M}_{\text{ob}}$ as

$$\hat{n}_{d,h} = \underset{k}{\text{argmax}} \mathbf{M}_{\text{ob}}(\hat{n}_{r,h}, k).$$

The high-RCS radar channel matrix $\hat{\boldsymbol{\Gamma}}_{\text{high}} \in \mathbb{C}^{N_r \times N_d}$ is zero everywhere, except at the locations where high-RCS targets are identified. At those locations

$$\hat{\boldsymbol{\Gamma}}_{\text{high}}(\hat{n}_{r,h}, \hat{n}_{d,h}) = \gamma_h. \tag{13}$$

In a scenario with multiple high-RCS targets, $\hat{\boldsymbol{\Gamma}}_{\text{high}}$ is updated according to (13) for each detected high-RCS target.

The radar channel corresponding to low-RCS targets can be estimated by masking out all the high-RCS targets as

$$\hat{\boldsymbol{\Gamma}}_{\text{low, SA}} = (\mathbf{M}_{\text{ob}} - \mathbf{M}_{\text{high}}) \odot \hat{\boldsymbol{X}}_{\text{ob, filt}} \tag{14}$$

where $\mathbf{M}_{\text{high}}$ is a binary mask matrix that is 1 only at the locations, where $\hat{\boldsymbol{\Gamma}}_{\text{high}} \neq 0$. The low-RCS radar channel estimate in (14), however, suffers from the scaling ambiguity issue due to one-bit sparse recovery. Specifically, the estimate $\hat{\boldsymbol{\Gamma}}_{\text{low, SA}}$ is accurate only up to a positive scaling. Our method resolves the scaling ambiguity issue using high-resolution measurements from the first slow-time slot.

To determine the scaling ambiguity in $\hat{\boldsymbol{\Gamma}}_{\text{low, SA}}$, the high-resolution returns from the low-RCS targets must be isolated. We extract these returns, denoted by $\boldsymbol{y}_{0,\text{low}}$, by eliminating the estimated returns from the high-RCS target from $\boldsymbol{y}_0$, i.e.,

$$\boldsymbol{y}_{0,\text{low}} = \boldsymbol{y}_0 - \boldsymbol{S}\hat{\boldsymbol{\Gamma}}_{\text{high}}\boldsymbol{a}_0.$$

Now, the high-resolution samples expected from the low-RCS targets can be expressed as $\delta \boldsymbol{S}\hat{\boldsymbol{\Gamma}}_{\text{low, SA}}\boldsymbol{a}_0$, where $\delta > 0$ is the unknown scaling. We find δ by minimizing the error between $\delta \boldsymbol{S}\hat{\boldsymbol{\Gamma}}_{\text{low, SA}}\boldsymbol{a}_0$ and $\boldsymbol{y}_{0,\text{low}}$, i.e.,

$$\hat{\delta} = \underset{\delta}{\text{argmin}} \left\| \boldsymbol{y}_{0,\text{low}} - \delta \boldsymbol{S}\hat{\boldsymbol{\Gamma}}_{\text{low, SA}}\boldsymbol{a}_0 \right\|_2^2. \tag{15}$$

Our channel estimate corresponding to the low-RCS targets is

$$\hat{\boldsymbol{\Gamma}}_{\text{low}} = \hat{\delta}\hat{\boldsymbol{\Gamma}}_{\text{low,SA}}.$$

Finally, our range-Doppler radar channel estimate is given by

$$\hat{\boldsymbol{\gamma}} = \text{vec}\left(\hat{\boldsymbol{\Gamma}}_{\text{low}} + \hat{\boldsymbol{\Gamma}}_{\text{high}}\right) \tag{16}$$

where $\hat{\boldsymbol{\gamma}}$ includes the reflection coefficients of both the high- and low-RCS targets. From Fig. 4(a) and (b), we observe that the low-RCS target is successfully detected using the proposed method, unlike in the conventional 1-bit system employing zero dither. Furthermore, when the Doppler of the high-RCS target is perfectly known, the dither signal provides a near-perfect cancellation of the return from the high-RCS target.

B. Case 2: Receiver Architecture for Known Doppler Statistics (Single High-RCS and Single Low-RCS Target)

In practice, the exact Doppler of targets may not be available. However, a probability distribution of the Doppler can be inferred based on the detected range (after matched filtering) and the lane topology. For example, a target detected 18 m

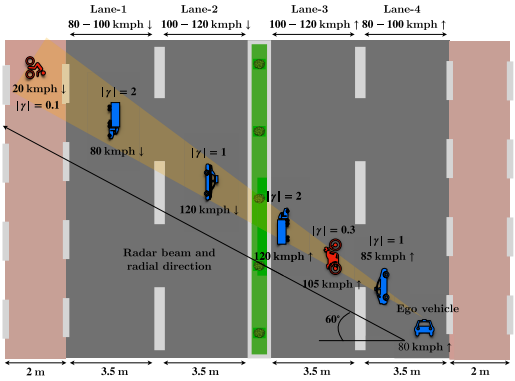

Fig. 5. Multilane highway scenario with targets of varying velocities and RCS values. We assume that the radar can isolate returns from any direction by beamforming. Under this assumption, the range estimate of the target can be used to determine its Doppler statistics based on the lane topology.

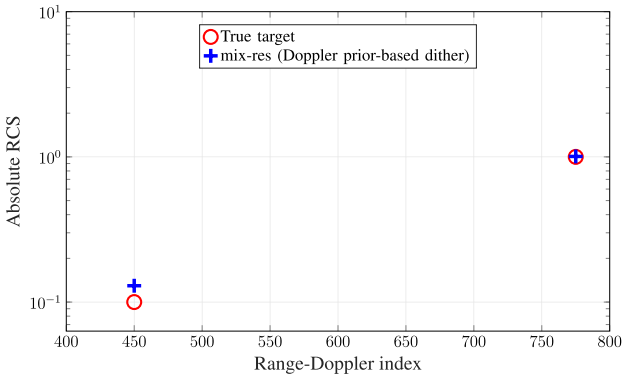

Fig. 6. Channel estimation for one high-RCS target with Doppler prior of size 4 and $|\gamma| = 1$, and one low-RCS target with $|\gamma| = 0.1$. Our proposed method can detect the low-RCS target even when the high-RCS target's Doppler is uncertain.

away from the ego vehicle along 60° in Fig. 5 occurs on lane where the speed limit is 80–100 km/h. The probability distribution of the Doppler of targets on this lane can be learned from a history of radar scans. In this article, we assume that this distribution is known to construct the dither signal.

We adapt the receiver system architecture in Fig. 2 to a scenario where the Doppler shift of the high-RCS target is modeled as a random variable ν_H with a known distribution $f(\nu_H)$. Then, our dither signal varies in the fast time as

$$\boldsymbol{q}_\ell[n] = \hat{\gamma}_H \boldsymbol{s}_{\hat{n}_{r,H}}[n]\, e^{j2\pi\nu_{d,H}[n]\ell} \tag{17}$$

where $\nu_H[n]$ is sampled at random according to $f(\nu_H)$. Note that the dither sample $\nu_H[n]$ is generated independently for each fast-time index. In the special case, when $f(\nu_H)$ is a Dirac delta distribution, the Doppler is perfectly known without any uncertainty, and (17) converges to the dither signal in (9). The dither vector $\boldsymbol{q}$ is constructed from (17) using (10). After applying the sparse recovery algorithm and scaling as per Section III-A, the channel estimate $\hat{\boldsymbol{\gamma}}$ is obtained. Fig. 6 shows the channel estimate when the high-RCS's Doppler statistics are uniformly distributed over four predetermined values, i.e., $\nu_H \sim \mathcal{U}\{0.1, 0.225, 0.25, 0.475\}$, with the actual Doppler associated with the target being 0.475. The remaining parameter values are identical to those in Section III-A. Despite the ambiguity in the high-RCS target's Doppler, the proposed method achieves significant suppression of the high-RCS target's response, enabling the detection of the low-RCS target. This demonstrates the robustness of the approach in handling Doppler uncertainties.

Note: We define Doppler prior length as the number of possible Doppler shifts for a high-RCS target, e.g., 4 for the prior used in Fig. 6. As we do not focus on learning the exact Doppler statistics, we assume a uniform distribution within lane topology-based Doppler limits. For example, if the Doppler prior length is 2 and the Doppler range is $\{\nu_a, \nu_b\}$, the Doppler distribution is $\mathcal{U}\{\nu_a, \nu_b\}$.

C. Proposed Dither Signal for a General Scenario

In a general case, we consider H number of high-RCS targets detected after matched filtering at $\ell = 0$. We use $f(\nu_{d,h})$ to denote the Doppler distribution of the hth target. In this scenario with multiple detected high-RCS signals, we propose to set the dither signal in slow-time slot ℓ to

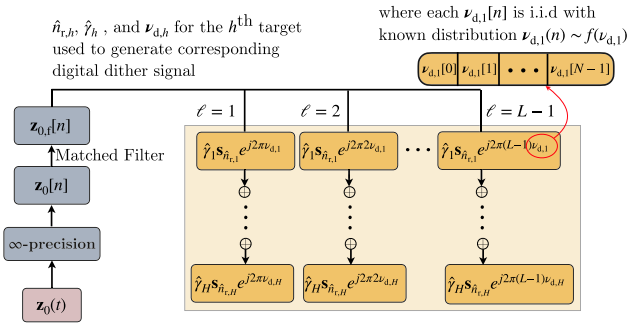

Fig. 7. For H identified high-RCS targets, the dither signal in our method is obtained by adding dithers for each high-RCS target using their Doppler statistics. The individual dithers are generated according to our procedure in Section III-B.

$$\boldsymbol{q}_\ell[n] = \sum_{h=1}^{H} \hat{\gamma}_h \boldsymbol{s}_{\hat{n}_{r,h}}[n]\, e^{j2\pi\nu_{d,h}[n]\ell} \tag{18}$$

where $\nu_{d,h}[n]$ is sampled at random from $f(\nu_{d,h})$. This dither signal shown in Fig. 7 is the sum of H different dither signals, each generated according to (17). Our channel estimation process for this scenario with multiple high-RCS targets remains the same as the one in Section III-A. Here, $\hat{\boldsymbol{\Gamma}}_{\text{high}}$ is a matrix with H nonzero entries instead of the one-sparse matrix in Section III-A.

Fig. 8(b) illustrates the channel estimate using proposed dithering for two high-RCS targets and one low-RCS target. Each high-RCS target has an absolute RCS value of 1 and the Doppler prior length 4, while the low-RCS target has an absolute RCS value of 0.1. The remaining parameter values are identical to those in Section III-A, with the exception of the sparsity-inducing parameter, which takes the value $\alpha = 110$ in this case. Despite the presence of multiple dominant scatterers, the proposed approach successfully suppresses the high-RCS responses, unmasking the weaker target. This demonstrates the scalability and effectiveness of the proposed architecture in complex scenarios with multiple high-RCS targets and uncertain Doppler shifts.

D. Our Low-Complexity Implementation of Sparse Recovery

To aid our low-complexity implementation, the $NL - N$ dimension measurement vector $\boldsymbol{y}$ is extended as $\boldsymbol{y}_{\mathrm{e}} = [\boldsymbol{0}_N; \boldsymbol{y}]$, where $\boldsymbol{0}_N$ is a zero vector of length N. Correspondingly, the matrix $\boldsymbol{A}$ is extended to an $L \times L$ matrix $\boldsymbol{A}_{\mathrm{e}} = [\boldsymbol{a}_0, \ldots, \boldsymbol{a}_{L-1}]$. The matrix $\boldsymbol{B}_{\mathrm{e}}$ is then derived from $\boldsymbol{A}_{\mathrm{e}}$ according to (3). The computational complexity of the sparse recovery iteration in (5) is dominated by the inversion of $\tilde{\boldsymbol{B}}_{\mathrm{e}}^{\mathrm{T}}\tilde{\boldsymbol{B}}_{\mathrm{e}} + \alpha\tilde{\boldsymbol{D}}^t$. The complexity to invert this $2 \times 2NL$ matrix scales as $\mathcal{O}(N^3L^3)$. For typical N and L in automotive applications, this cubic scaling makes sparse recovery using (5) computationally expensive.

We select the transmit sequence $\boldsymbol{s}$ and steering matrix $\boldsymbol{A}_{\mathrm{e}}$ so that $\tilde{\boldsymbol{B}}_{\mathrm{e}}^{\mathrm{T}}\tilde{\boldsymbol{B}}_{\mathrm{e}} + \alpha\tilde{\boldsymbol{D}}^t$ becomes diagonal. To motivate our choice, we write

$$\tilde{\boldsymbol{B}}_{\mathrm{e}}^{\mathrm{T}}\tilde{\boldsymbol{B}}_{\mathrm{e}} = \begin{bmatrix} \Re\left(\boldsymbol{B}_{\mathrm{e}}^{\mathrm{H}}\boldsymbol{B}_{\mathrm{e}}\right) & -\Im\left(\boldsymbol{B}_{\mathrm{e}}^{\mathrm{H}}\boldsymbol{B}_{\mathrm{e}}\right) \\ \Im\left(\boldsymbol{B}_{\mathrm{e}}^{\mathrm{H}}\boldsymbol{B}_{\mathrm{e}}\right) & \Re\left(\boldsymbol{B}_{\mathrm{e}}^{\mathrm{H}}\boldsymbol{B}_{\mathrm{e}}\right) \end{bmatrix}$$

where the real and imaginary parts of $\boldsymbol{B}_{\mathrm{e}}^{\mathrm{H}}\boldsymbol{B}_{\mathrm{e}}$ are

$$\begin{aligned} \Re\left(\boldsymbol{B}_{\mathrm{e}}^{\mathrm{H}}\boldsymbol{B}_{\mathrm{e}}\right) &= \left(\boldsymbol{A}_{\mathrm{e}\Re}\boldsymbol{A}_{\mathrm{e}\Re}^{\mathrm{T}} + \boldsymbol{A}_{\mathrm{e}\Im}\boldsymbol{A}_{\mathrm{e}\Im}^{\mathrm{T}}\right) \otimes \left(\boldsymbol{S}_{\Re}^{\mathrm{T}}\boldsymbol{S}_{\Re} + \boldsymbol{S}_{\Im}^{\mathrm{T}}\boldsymbol{S}_{\Im}\right) \\ \Im\left(\boldsymbol{B}_{\mathrm{e}}^{\mathrm{H}}\boldsymbol{B}_{\mathrm{e}}\right) &= \left(\boldsymbol{A}_{\mathrm{e}\Re}\boldsymbol{A}_{\mathrm{e}\Re}^{\mathrm{T}} + \boldsymbol{A}_{\mathrm{e}\Im}\boldsymbol{A}_{\mathrm{e}\Im}^{\mathrm{T}}\right) \otimes \left(\boldsymbol{S}_{\Re}^{\mathrm{T}}\boldsymbol{S}_{\Im} - \boldsymbol{S}_{\Im}^{\mathrm{T}}\boldsymbol{S}_{\Re}\right). \end{aligned}$$

Now, we assume $N_r = N$, $N_d = L$, and set the Doppler grid for (2) as $\boldsymbol{\nu}_{\mathrm{grid}} = [0, 1/L, \ldots, (L-1)/L]$. With this choice, $\boldsymbol{A}_{\mathrm{e}}$ is L times the inverse DFT matrix and $(\boldsymbol{A}_{\mathrm{e}\Re}\boldsymbol{A}_{\mathrm{e}\Re}^{\mathrm{T}} + \boldsymbol{A}_{\mathrm{e}\Im}\boldsymbol{A}_{\mathrm{e}\Im}^{\mathrm{T}})$ is hence diagonal. Next, we set $\boldsymbol{s}$ to a Zadoff–Chu (ZC) sequence $s[n] = \exp(-j\pi n^2/N)$ so that $(\boldsymbol{S}_{\Re}^{\mathrm{T}}\boldsymbol{S}_{\Re} + \boldsymbol{S}_{\Im}^{\mathrm{T}}\boldsymbol{S}_{\Im})$ is diagonal, while $(\boldsymbol{S}_{\Re}^{\mathrm{T}}\boldsymbol{S}_{\Im} - \boldsymbol{S}_{\Im}^{\mathrm{T}}\boldsymbol{S}_{\Re})$ is zero. This is due to the fact that the ZC sequence is orthogonal to its circularly shifted version. In summary, our design makes $\tilde{\boldsymbol{B}}_{\mathrm{e}}^{\mathrm{T}}\tilde{\boldsymbol{B}}_{\mathrm{e}} + \alpha\tilde{\boldsymbol{D}}^t$ diagonal and thus reduces the cost of computing its inverse from $\mathcal{O}(N^3L^3)$ to $\mathcal{O}(NL)$.

Our choice of $N_r = N$ and $\boldsymbol{A}_{\mathrm{e}}$ also aids fast matrix-vector multiplication in $\tilde{\boldsymbol{B}}_e^{\mathrm{T}}\tilde{\boldsymbol{x}}$, an operation in (5) for $\tilde{\boldsymbol{x}} = \tilde{\boldsymbol{g}}^t + \eta\tilde{\boldsymbol{q}}$. This speed-up is achieved using the fast Fourier transform (FFT), denoted by the operator $\mathcal{F}(\cdot)$, and its inverse operator $\mathcal{F}^{-1}(\cdot)$. For matrices, we define the row-wise FFT operator as $\mathcal{F}_{\mathrm{row}}(\cdot)$ and the column-wise FFT operator as $\mathcal{F}_{\mathrm{col}}(\cdot)$, with corresponding notations for their inverses. Due to the circulant structure of $\boldsymbol{S}$ and the inverse DFT $\boldsymbol{A}_{\mathrm{e}}$, the matrix-vector multiplication can be computed using

$$\begin{aligned} \boldsymbol{B}_{\mathrm{e}}^{\mathrm{H}}\boldsymbol{x} &= L\,\mathrm{vec}\left[\mathcal{F}_{\mathrm{col}}\left(\mathrm{diag}\left(\left(\mathcal{F}\left(\boldsymbol{s}^*\right)\right)\right)\right) \cdot \mathcal{F}_{\mathrm{col}}^{-1}\left(\mathcal{F}_{\mathrm{row}}\left(\boldsymbol{X}\right)\right)\right] \\ \tilde{\boldsymbol{B}}_{\mathrm{e}}^{\mathrm{T}}\tilde{\boldsymbol{x}} &= \left[\Re\left(\boldsymbol{B}_{\mathrm{e}}^{\mathrm{H}}\boldsymbol{x}\right); \Im\left(\boldsymbol{B}_{\mathrm{e}}^{\mathrm{H}}\boldsymbol{x}\right)\right] \end{aligned}$$

where $\boldsymbol{X}$ is the $N \times L$ matrix obtained by reshaping $NL \times 1$ vector $\boldsymbol{x}$. With our implementation, the computational complexity of the update in (5) is dominated by the matrix-vector multiplication step. Our design choice reduces its computational complexity from $\mathcal{O}(N^3L^3)$ to $\mathcal{O}(NL\log(N^2L))$.

E. Possible Directions to Address Limitations of Our Work

We now discuss the limitations of our work and possible research directions to address them. First, our approach does not leverage the matched filter's output as side information while solving the one-bit sparse recovery problem in Section II-B. To see how this side information can be derived, observe that the matched filtered output indicates the range bins associated with high-RCS targets, with the only ambiguity being the Doppler associated with those targets. This information, together with the Doppler statistics, can be used as a soft prior to encourage nonzero entries at the locations where high-RCS targets are likely to occur.

Second, our approach also assumes that the generated dither signal temporally aligns with the return from the high-RCS target on a fast-time scale. In practice, however, the two signals are not perfectly aligned in time, with the misalignment typically being a fraction of the fast-time interval. We do not study the impact of temporal misalignment in this article. A possible approach to compensate for this misalignment is to introduce an analog true-time delay element in the received signal chain. Developing true-time delay compensation algorithms with the mixed-resolution ADC receiver is beyond the scope of this article.

Third, our approach assumes pencil beam transmission, resulting in no more than one target per range bin. In practice, however, the beams have a finite beamwidth, due to which multiple targets may be present in each range bin. In such a setting, our dithering strategy can remain unchanged, while our radar channel estimation algorithm must be modified to account for multiple targets. For example, this can be achieved by replacing (11) with a constant false alarm rate (CFAR) detector to account for multiple targets in a range bin. Then, the RCS of strong targets can be estimated using a mixed-resolution measurement model instead of (13). Finally, the radar channel comprising low-RCS targets and high-RCS targets can be combined similarly to (16).

IV. Performance Analysis of Low-RCS Target Detection Under Dithering

We consider a two-target scenario to analyze the probability of detecting the low-RCS target as a function of the dither signal. Here, our emphasis is only on low-RCS target detection, which is challenging due to one-bit measurements. To aid a tractable analysis, we consider the Neyman–Pearson (NP) detector instead of the one-bit sparse recovery in Section II-B. Our simulations in Section VI, however, are based on more complex scenarios where we use one-bit sparse recovery. Using our analysis, we study detection with the proposed dither signal as a function of the dynamic range and the number of measurements.

From (3), we observe that the return from a target in a specific range-Doppler bin is proportional to the corresponding column in $\boldsymbol{B}$. We assume that the high-RCS target is at the range-Doppler bin corresponding to column c_1 in $\boldsymbol{B}$ and the low-RCS target is at the bin associated with column c_2. For simplicity, we set the high-RCS target's RCS as 1 and the low-RCS target's RCS as a real-value γ. In our method, the high-RCS target is detected using high-precision measurements from the first slow-time interval ($\ell = 0$) using matched filtering. Assuming that the high-RCS target has been detected, we focus on low-RCS target detection using the subsequent one-bit measurements $\tilde{\boldsymbol{y}}$ acquired with a dither signal $\boldsymbol{q}$.

To study low-RCS target detection from $\tilde{\boldsymbol{y}}$, we employ the following binary hypothesis testing model:

$$\begin{cases}\mathcal{H}_0 : \tilde{\boldsymbol{y}}\left(\tilde{\boldsymbol{q}}\right) = \operatorname{sign}\left(\tilde{\boldsymbol{\tau}}_0\left(\tilde{\boldsymbol{q}}\right)\right) \\ \mathcal{H}_1 : \tilde{\boldsymbol{y}}\left(\tilde{\boldsymbol{q}}\right) = \operatorname{sign}\left(\tilde{\boldsymbol{\tau}}_1\left(\tilde{\boldsymbol{q}}\right)\right)\end{cases}$$

where $\tilde{\boldsymbol{\tau}}_0(\tilde{\boldsymbol{q}}) = \tilde{\boldsymbol{b}}_{c_1}^{\mathrm{T}} + \tilde{\boldsymbol{e}} - \tilde{\boldsymbol{q}}$, and $\tilde{\boldsymbol{\tau}}_1(\tilde{\boldsymbol{q}}) = \tilde{\boldsymbol{b}}_{c_1}^{\mathrm{T}} + \gamma\tilde{\boldsymbol{b}}_{c_0}^{\mathrm{T}} + \tilde{\boldsymbol{e}} - \tilde{\boldsymbol{q}}$.

The likelihood ratio test in an NP detector is

$$\mathcal{T}\left(\tilde{\boldsymbol{y}}\left(\tilde{\boldsymbol{q}}\right)\right) = \frac{f_1\left(\tilde{\boldsymbol{y}}\left(\tilde{\boldsymbol{q}}\right)\right)}{f_0\left(\tilde{\boldsymbol{y}}\left(\tilde{\boldsymbol{q}}\right)\right)} \underset{\mathcal{H}_0}{\overset{\mathcal{H}_1}{\gtrless}} \kappa$$

where $f_1(\tilde{\boldsymbol{y}}, \tilde{\boldsymbol{q}})$ and $f_0(\tilde{\boldsymbol{y}}, \tilde{\boldsymbol{q}})$ denote the pdfs under hypothesis $\mathcal{H}_1$ and $\mathcal{H}_0$, respectively. For this detector, we derive the probability of false alarm $\mathcal{P}_{\mathrm{FA}}$ and the probability of detection $\mathcal{P}_{\mathcal{D}}$ as a function of $\tilde{\boldsymbol{q}}$

$$\mathcal{P}_{\mathrm{FA}}\left(\tilde{\boldsymbol{q}}\right) = 1 - \Phi\left(\frac{\tilde{\xi}\left(\tilde{\boldsymbol{q}}\right) - \mu_0\left(\tilde{\boldsymbol{q}}\right)}{\sigma_0\left(\tilde{\boldsymbol{q}}\right)}\right) \tag{19}$$

$$\mathcal{P}_{\mathcal{D}}\left(\tilde{\boldsymbol{q}}\right) = 1 - \Phi\left(\frac{\tilde{\xi}\left(\tilde{\boldsymbol{q}}\right) - \mu_1\left(\tilde{\boldsymbol{q}}\right)}{\sigma_1\left(\tilde{\boldsymbol{q}}\right)}\right) \tag{20}$$

where $\mu_i(\tilde{\boldsymbol{q}})$ and $\sigma_i^2(\tilde{\boldsymbol{q}})$ for $i = \{0, 1\}$ are defined as follows:

$$\mu_i\left(\tilde{\boldsymbol{q}}\right) = \sum_{m=1}^{2NL}\left(1 - 2\Phi\left(\frac{-\sqrt{2}\tau_{i,m}\left(\tilde{\boldsymbol{q}}_m\right)}{\sigma}\right)\right)$$

$$\sigma_i^2\left(\tilde{\boldsymbol{q}}\right) = 4\sum_{m=1}^{2NL}\Phi\left(\frac{-\sqrt{2}\tau_{i,m}\left(\tilde{\boldsymbol{q}}_m\right)}{\sigma}\right) \times\left(1 - \Phi\left(\frac{-\sqrt{2}\tau_{i,m}\left(\tilde{\boldsymbol{q}}_m\right)}{\sigma}\right)\right)\boldsymbol{\rho}_m^2\left(\tilde{\boldsymbol{q}}_m\right)$$

where $\boldsymbol{\rho}_m(\tilde{\boldsymbol{q}}_m)$ and $\tilde{\xi}(\tilde{\boldsymbol{q}})$ are given by

$$\boldsymbol{\rho}_m\left(\tilde{\boldsymbol{q}}_m\right) = \ln\frac{\Phi\left(\frac{-\sqrt{2}\tilde{\tau}_{1,m}\left(\tilde{\boldsymbol{q}}_m\right)}{\sigma}\right)}{\Phi\left(\frac{-\sqrt{2}\tilde{\tau}_{0,m}\left(\tilde{\boldsymbol{q}}_m\right)}{\sigma}\right)} + \ln\frac{1 - \Phi\left(\frac{-\sqrt{2}\tilde{\tau}_{1,m}\left(\tilde{\boldsymbol{q}}_m\right)}{\sigma}\right)}{1 - \Phi\left(\frac{-\sqrt{2}\tilde{\tau}_{0,m}\left(\tilde{\boldsymbol{q}}_m\right)}{\sigma}\right)}$$

$$\tilde{\xi}\left(\tilde{\boldsymbol{q}}\right) = 2\ln\kappa - \sum_{m=1}^{2NL}\ln\frac{\Phi\left(\frac{-\sqrt{2}\tilde{\tau}_{1,m}\left(\tilde{\boldsymbol{q}}_m\right)}{\sigma}\right)}{\Phi\left(\frac{-\sqrt{2}\tilde{\tau}_{0,m}\left(\tilde{\boldsymbol{q}}_m\right)}{\sigma}\right)} - \sum_{m=1}^{2NL}\ln\frac{1 - \Phi\left(\frac{-\sqrt{2}\tilde{\tau}_{1,m}\left(\tilde{\boldsymbol{q}}_m\right)}{\sigma}\right)}{1 - \Phi\left(\frac{-\sqrt{2}\tilde{\tau}_{0,m}\left(\tilde{\boldsymbol{q}}_m\right)}{\sigma}\right)}.$$

Proof: See Appendix A. ∎

As our method draws the dither signal from a distribution, we compute the probability of detection by averaging the expression in (20) for several realizations of $\tilde{\boldsymbol{q}}$ in (18). For $N = L = 24$, $N_r = N$, $N_d = L$, and SNR = 20 dB, the probability of detection for the proposed method with Doppler prior lengths of 1 (known Doppler), 2, and 12 is compared to conventional one-bit radars in Fig. 9. In addition to the zero thresholding in 1-bit, we compare our method against two uniform random dithering techniques:

A. Uniform Random Dithering [17]

In this case, 1-bit quantization is performed in all slow-time slots, including the first slot. The dither signal for each pair of ℓ and n is drawn from i.i.d. uniform distribution, i.e., $\tilde{\boldsymbol{q}}_\ell[n] \sim \mathcal{U}[-1, 1]$.

B. Power Adjusted Uniform Random Dithering

Our approach uses a high-resolution at the ADC in the first slow-time slot, unlike [17], which uses 1-bit ADCs throughout. For a fair comparison, we adapt the technique in [17] to the ADC resolution profile in this article. We call this benchmark as power-adjusted uniform random dithering. In this benchmark, the power associated with the high-RCS targets, denoted as p_H, is estimated from the matched filter output in (8).

A dither signal with entries drawn from $\mathcal{U}[-1, 1]$ is effective when the power of high-RCS targets is comparable to the dither signal's power, i.e., 1/3. This is because the average power of $\mathcal{U}[-1, 1]$ is 1/3. When the power p_H is substantially different from 1/3, the uniform dithering technique becomes less effective. The power-adjusted uniform random dithering benchmark generates a dither signal whose power is comparable to p_H. This is achieved by drawing the dither signal entries according to $\boldsymbol{q}_\ell[n] \sim \mathcal{U}[-(3p_H)^{1/2}, (3p_H)^{1/2}]$. The choice of the limits $-(3p_H)^{1/2}$ and $(3p_H)^{1/2}$ ensures that the average power of the dither signal matches the high-RCS signal power p_H.

1) Evaluating Various Dithering Methods Using $\mathcal{P}_{\mathcal{D}}$ in (20): When the absolute RCS of the weak target drops to 0.1, its return signal power becomes comparable to the noise power at an SNR of 20 dB and falls below the noise level as the RCS decreases further. A significant improvement in $\mathcal{P}_{\mathcal{D}}$ is observed when the SNR for the weak target's return signal falls below 0 dB. This improvement is achieved using the proposed mixed-resolution architecture with Doppler prior-based dithering, compared to the conventional one-bit radar system, a one-bit system with uniform dither, and a mixed-resolution system with power-adjusted uniform dither. For instance, when the absolute RCS value of the low-RCS target is 0.07, the proposed method achieves a 95% probability of detection for a Doppler prior length of 12. This is substantially higher than 64% with a one-bit system with no dithering.

We also observe from Fig. 9 that the detection probability for the proposed method increases to 99.95% and 99.99% as the Doppler prior length decreases to 2 and 1, respectively. As the Doppler prior length increases—indicating greater uncertainty—the detection performance degrades. However, even with larger Doppler priors, the proposed method significantly enhances the dynamic range by leveraging the probability distribution of the Doppler, ensuring a higher probability of detecting low-RCS targets.

Finally, increasing the number of measurements enhances the ability to distinguish between noise and weak targets. This relationship is illustrated in Fig. 10, where increasing N and L while keeping all other parameters constant, improves $\mathcal{P}_{\mathcal{D}}$. To achieve detection comparable to an infinite resolution system with a grid size of 10×10, the proposed architecture requires a grid size of 30×30, compared to 70×70 for a one-bit system with zero thresholds. This demonstrates that by adapting the ADC resolution and designing a situation-aware dither signal, the dynamic range can be substantially improved while requiring significantly fewer measurements than conventional one-bit systems.

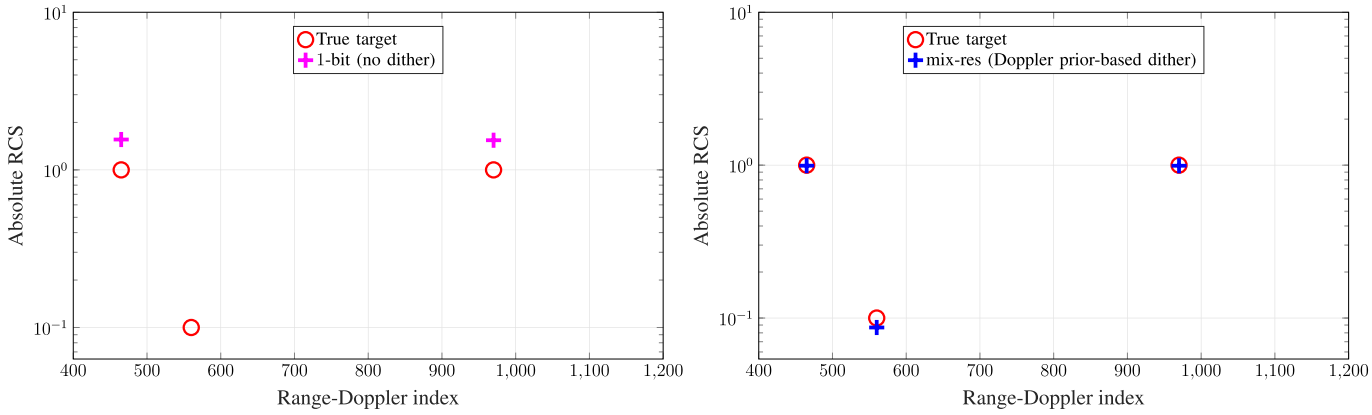

Fig. 8. Channel estimation for two high-RCS targets with Doppler prior of length 4 and $|\gamma| = 1$ each and one low-RCS target with $|\gamma| = 0.1$. The dither signal generated with our method facilitates low-RCS target detection, even under Doppler uncertainty on the high-RCS targets. The conventional one-bit system using a zero dither fails to detect the low-RCS target. (a) Conventional one-bit system. (b) Proposed mixed-resolution system with a Doppler prior (length 4).

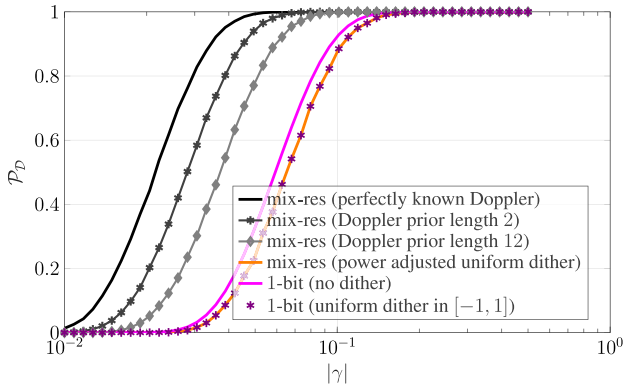

Fig. 9. Comparison of probability of detection $\mathcal{P}_\mathcal{D}$ for a grid size $N \times L = 24 \times 24$ for different dithering signals and receiver designs. As expected, $\mathcal{P}_\mathcal{D}$ is higher when the uncertainty on the high-RCS target's Doppler is low.

V. CRB for Low-RCS Target Parameter Estimation

In this section, we study the Cramér–Rao bound (CRB) for weak targets' RCS estimation. In conventional one-bit systems without dithering, the strong target saturates the quantizer, which severely degrades the Fisher information available for the weak target. In contrast, the use of situation-aware dithering alleviates saturation by suppressing the dominant target's contribution to the quantized measurements, thereby enhancing the dynamic range for the weak target.

For the mixed-resolution framework considered in this article, the Fisher information matrix (FIM) is computed using both the high-resolution measurements from the initial slow-time slot and the subsequent dithered one-bit measurements. A formulation of the FIM for mixed-resolution radar systems was previously derived in [10] in the context of MIMO radar with a spatial array of mixed-resolution ADCs. We apply the result from [10] to a single-antenna system with an ADC whose resolution varies temporally. Using the approach in [10], the FIM in our setting can be expressed as

$$\mathrm{FIM}(\boldsymbol{q}) = \mathrm{UQFIM} + \mathrm{QFIM}(\boldsymbol{q}) \tag{21}$$

where UQFIM is the FIM from the unquantized measurements and is given by

$$\mathrm{UQFIM} = \frac{2}{\sigma^2}\tilde{\boldsymbol{B}}_U^{\mathrm{T}}\tilde{\boldsymbol{B}}_U \tag{22}$$

where

$$\tilde{\boldsymbol{B}}_{\mathrm{U}} = \begin{bmatrix} \Re\left(\boldsymbol{a}_0^{\mathrm{T}} \otimes \boldsymbol{S}\right) & -\Im\left(\boldsymbol{a}_0^{\mathrm{T}} \otimes \boldsymbol{S}\right) \\ \Im\left(\boldsymbol{a}_0^{\mathrm{T}} \otimes \boldsymbol{S}\right) & \Re\left(\boldsymbol{a}_0^{\mathrm{T}} \otimes \boldsymbol{S}\right) \end{bmatrix}.$$

The term QFIM($\boldsymbol{q}$) corresponds to the Fisher information from the quantized measurements and is given by [38]

$$\begin{aligned}\mathrm{QFIM}_{i,j}(\boldsymbol{q}) = &\frac{2}{\sigma^2}\tilde{\boldsymbol{B}}_{Q,0}^{\mathrm{T}}\left(\boldsymbol{g}_\Re(\boldsymbol{q}) \odot \tilde{\boldsymbol{B}}_{Q,0}\right) \\ &+ \frac{2}{\sigma^2}\tilde{\boldsymbol{B}}_{Q,1}^{\mathrm{T}}\left(\boldsymbol{g}_\Im(\boldsymbol{q}) \odot \tilde{\boldsymbol{B}}_{Q,1}\right)\end{aligned}$$

where

$$\boldsymbol{g}_\Re(m,\boldsymbol{q}) = \frac{\varphi^2\left(\frac{\Re(\boldsymbol{b}_m^{\mathrm{T}}\boldsymbol{\gamma}) - \boldsymbol{q}_\Re}{\sqrt{\sigma^2/2}}\right)}{\Phi\left(\frac{\Re(\boldsymbol{b}_m^{\mathrm{T}}\boldsymbol{\gamma}) - \boldsymbol{q}_\Re}{\sqrt{\sigma^2/2}}\right)\Phi\left(\frac{-\Re(\boldsymbol{b}_m^{\mathrm{T}}\boldsymbol{\gamma}) + \boldsymbol{q}_\Re}{\sqrt{\sigma^2/2}}\right)}$$

$$\boldsymbol{g}_\Im(m,\boldsymbol{q}) = \frac{\varphi^2\left(\frac{\Im(\boldsymbol{b}_m^{\mathrm{T}}\boldsymbol{\gamma}) - \boldsymbol{q}_\Im}{\sqrt{\sigma^2/2}}\right)}{\Phi\left(\frac{\Im(\boldsymbol{b}_m^{\mathrm{T}}\boldsymbol{\gamma}) - \boldsymbol{q}_\Im}{\sqrt{\sigma^2/2}}\right)\Phi\left(\frac{-\Im(\boldsymbol{b}_m^{\mathrm{T}}\boldsymbol{\gamma}) + \boldsymbol{q}_\Im}{\sqrt{\sigma^2/2}}\right)}$$

and

$$\begin{aligned}\tilde{\boldsymbol{B}}_{\mathrm{Q},0} &= \left[\Re(\tilde{\boldsymbol{B}})\ -\Im(\tilde{\boldsymbol{B}})\right] \\ \tilde{\boldsymbol{B}}_{\mathrm{Q},1} &= \left[\Im(\tilde{\boldsymbol{B}})\ \Re(\tilde{\boldsymbol{B}})\right].\end{aligned}$$

The corresponding CRB matrix is then obtained by inverting the FIM as

$$\mathrm{CRB}(\boldsymbol{q}) = \mathrm{FIM}^{-1}(\boldsymbol{q}). \tag{23}$$

The diagonal entries of the CRB matrix provide lower bounds on the variances of the estimation errors for the RCS values of targets in each range-Doppler bin. For a target located at range bin n_r and Doppler bin n_d, the corresponding CRB entry for its RCS estimate is given by the $((n_r - 1)N_D + n_d)$th element in the diagonal of the CRB matrix. In our setup, we compute the CRB for the low-RCS targets by summing the

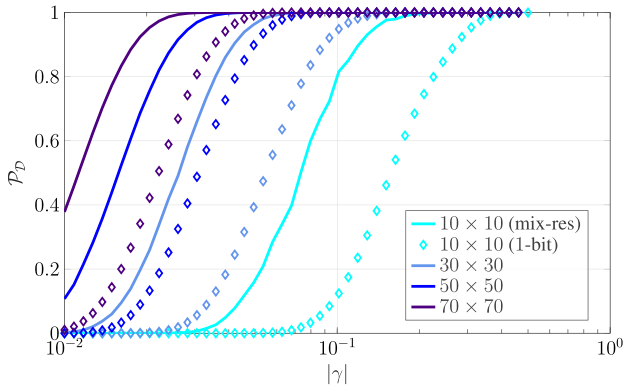

Fig. 10. Comparison of probability of detection $\mathcal{P}_\mathcal{D}$ for different grid sizes $N \times L$ for proposed mixed-resolution system architecture and Doppler prior length 4. Our system outperforms a conventional one-bit receiver using zero dither.

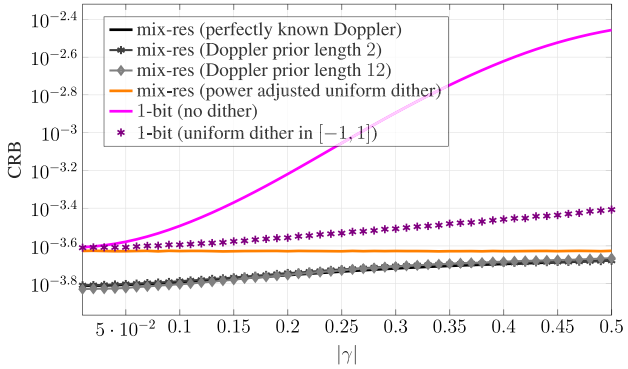

Fig. 11. CRB for RCS estimation of the weak target in the presence of one dominant target, for different dithers and receiver designs. Here, the grid size $N \times L = 24 \times 24$.

diagonal entries corresponding to their range-Doppler indices. The total CRB for the weak targets is therefore given by the sum of the relevant entries in CRB($\boldsymbol{q}$). In Figs. 11 and 12, we plot the CRB corresponding to the weak target in a scenario with one high-RCS and one low-RCS target to highlight the performance gains achieved by our proposed situation-aware dithering and mixed-resolution strategy.

Figs. 11 and 12 illustrate that the proposed mixed-resolution architecture consistently achieves a lower CRB for the weak target's RCS across various dithering strategies and grid sizes. This confirms that, even in the presence of dominant targets and coarse quantization, incorporating a small number of high-resolution samples significantly improves the lower bound on estimation accuracy. It is important to interpret these estimation bounds in conjunction with the probability of detection results shown in Figs. 9 and 10. Our CRB for RCS estimation is conditioned on successful target detection. In low-SNR or highly masked regimes, where the probability of detection is low, the relevance of the CRB as a performance benchmark diminishes. Therefore, the CRB study is particularly meaningful when viewed alongside the detection curves in Fig. 9.

VI. Simulation Results

The probability of detection, while essential, does not provide a comprehensive performance metric, as it only quantifies the detectability of a weak target. For a more comprehensive

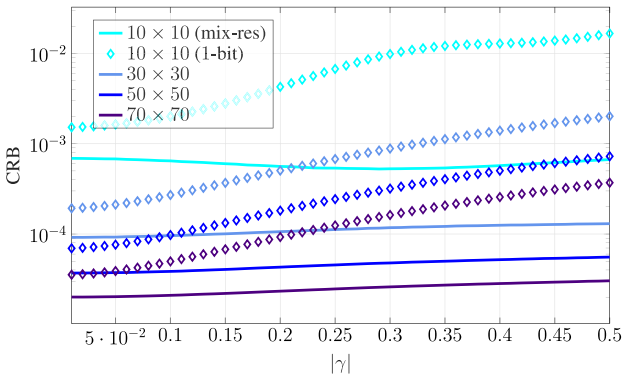

Fig. 12. CRB for RCS estimation of the weak target in the presence of one dominant target, for different grid sizes $N \times L$. Here, we consider our proposed mixed-resolution architecture with a Doppler prior length of 4.

TABLE I
Simulation Parameters

Parameter Name	Symbol	Value
Carrier frequency	f_c	80 GHz
Bandwidth	B	0.15 GHz
Chip duration	Ts	6.67 ns
Range resolution	r_{res}	1 m
Pulse duration	T_p	NT_s
Doppler resolution	d_{res}	$1/LT_\text{p}$
SNR	–	20 dB

performance analysis, we also evaluate the NMSE of the radar channel associated with the low-RCS targets, i.e.,

$$\text{NMSE} = 10\log_{10}\frac{\left\|\boldsymbol{\Gamma}_{\text{true}} \odot \left(\mathbf{M}_{\text{ob}} - \mathbf{M}_{\text{high}}\right) - \hat{\boldsymbol{\Gamma}}_{\text{low}}\right\|_2^2}{\left\|\boldsymbol{\Gamma}_{\text{true}} \odot \left(\mathbf{M}_{\text{ob}} - \mathbf{M}_{\text{high}}\right)\right\|_2^2}$$

where $\boldsymbol{\Gamma}_{\text{true}}$ represents the ground-truth range-Doppler matrix.

The NMSE is evaluated for the scenarios discussed in Sections III-A and III-C. The average NMSE with respect to the dither signal is computed by running the estimation algorithm over 1000 instances, each instance generating an independent realization of the dither signal, and finally taking an average. The simulation parameters that remain constant across all scenarios are summarized in Table I, while scenario-specific variable parameters are detailed during the discussion. For all scenarios, the absolute RCS value of the low-RCS target is varied between 0.01 and 0.5 to evaluate system performance across a range of target strengths. In addition, we present channel estimation results for a practical automotive scenario in Section VI-C.

A. Scenario 1: One High, One Low-RCS Target

This scenario involves one high-RCS target with an absolute RCS value of 1 and one low-RCS target. Fig. 13 illustrates the NMSE of the channel with respect to the absolute RCS value of the low-RCS target, estimated using the proposed mixed-resolution architecture with various Doppler prior lengths. The results are compared against a conventional one-bit system with zero and uniformly distributed thresholds, and a mixed-resolution architecture with power-adjusted uniform thresholds for $N = L = 24$ and $\alpha = 70$.

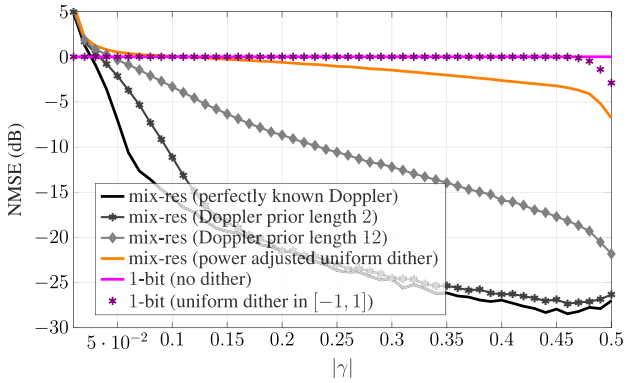

Fig. 13. Comparison of NMSE in the estimated RCS of the weak target in the presence of one dominant target for a grid size $N \times L = 24 \times 24$ for different dithering signals and receiver designs.

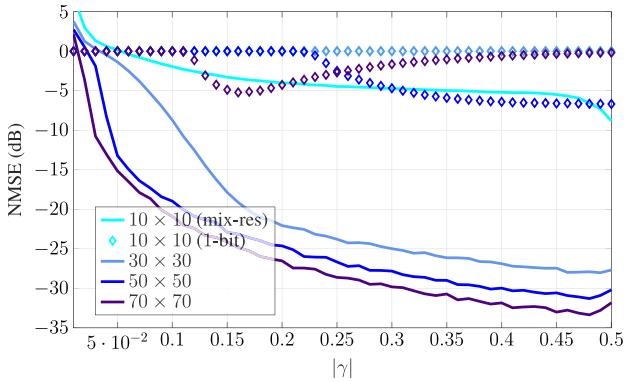

Fig. 14. Comparison of NMSE in the estimated RCS of the weak target in the presence of one dominant target for different grid sizes $N \times L$ for the proposed mixed-resolution system architecture and Doppler prior length 4.

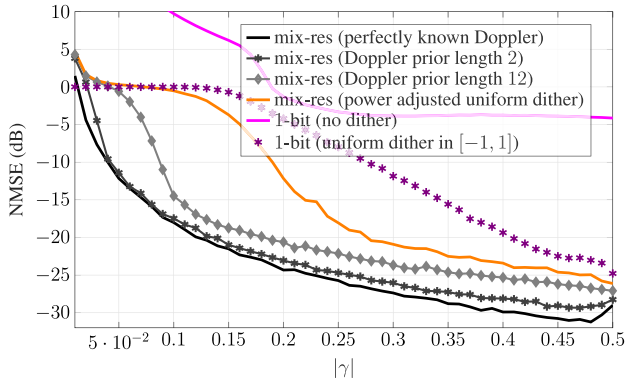

Fig. 15. Comparison of NMSE in the estimated RCS of the weak target in the presence of two dominant targets for a grid size $N \times L = 40 \times 40$ for different dithering signals and receiver designs.

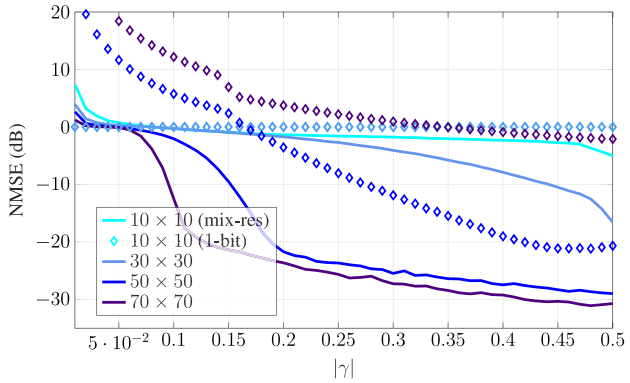

Fig. 16. Comparison of NMSE in the estimated RCS of the weak target in the presence of two dominant targets for different grid sizes $N \times L$ for the proposed mixed-resolution system architecture and Doppler prior length 4.

As evident from Fig. 9, the proposed mixed-resolution system provides superior RCS estimates compared to zero and different uniform dithering. Even with a Doppler prior length of 12, the proposed architecture, combined with Doppler-prior-based dithering, outperforms the conventional one-bit system with zero and uniformly distributed thresholds, as well as the mixed-resolution architecture with power-adjusted uniform thresholds both in terms of detection capability and accuracy of detection. Furthermore, Fig. 14 shows the NMSE across varying fast-time and slow-time pulse lengths for a Doppler prior length of 4. These results demonstrate that the proposed method not only requires fewer measurements for better detectability compared to other dithering strategies but also achieves significantly better estimation accuracy.

B. Scenario 2: Two High, One Low-RCS Targets

This scenario builds on the previous setup by introducing two high-RCS targets, each with an absolute RCS value of 1, in addition to one low-RCS target. Fig. 15 shows the NMSE performance for this configuration, with system parameters set to $N = L = 40$ and $\alpha = 60$. In this case, a Doppler prior of length 4 is assigned to each high-RCS target.

As seen in Fig. 15, the proposed mixed-resolution architecture continues to outperform the conventional one-bit system with zero and uniformly distributed thresholds, as well as the mixed-resolution system with power-adjusted uniform thresholds. Notably, even with two high-RCS targets, our Doppler prior-based dithering enables a more accurate estimation of the weak target's RCS. Fig. 16 shows NMSE for different numbers of radar channel measurements, i.e., NL. The proposed method outperforms the benchmarks while requiring fewer measurements than other dithering techniques.

C. Scenario 3: Lane Topology-Based Priors

Fig. 5 illustrates a multilane highway scenario, where an ego vehicle with a radar, traveling at 80 km/h, detects multiple targets with the radar beam directed at a 60° angle.

We demonstrate this scenario to emphasize the effectiveness of estimating channel parameters for weak targets in the presence of dominant reflections from high-RCS targets, particularly under conditions with varying Doppler priors. Using the lane topology in Fig. 5, the Doppler priors are assigned based on the range estimates from matched filtering.

The channel estimation results demonstrate the robustness of the proposed mixed-resolution architecture in such complex conditions. The cyclist, with $|\gamma| = 0.1$, represents a low-RCS target with a weak return signal, which is particularly challenging to detect amidst strong reflections from high-RCS targets such as trucks and cars. With $N \times L = 450 \times 450$, conventional one-bit radar systems can detect the cyclist and similar weak targets. However, as seen in Fig. 17(a), the one-

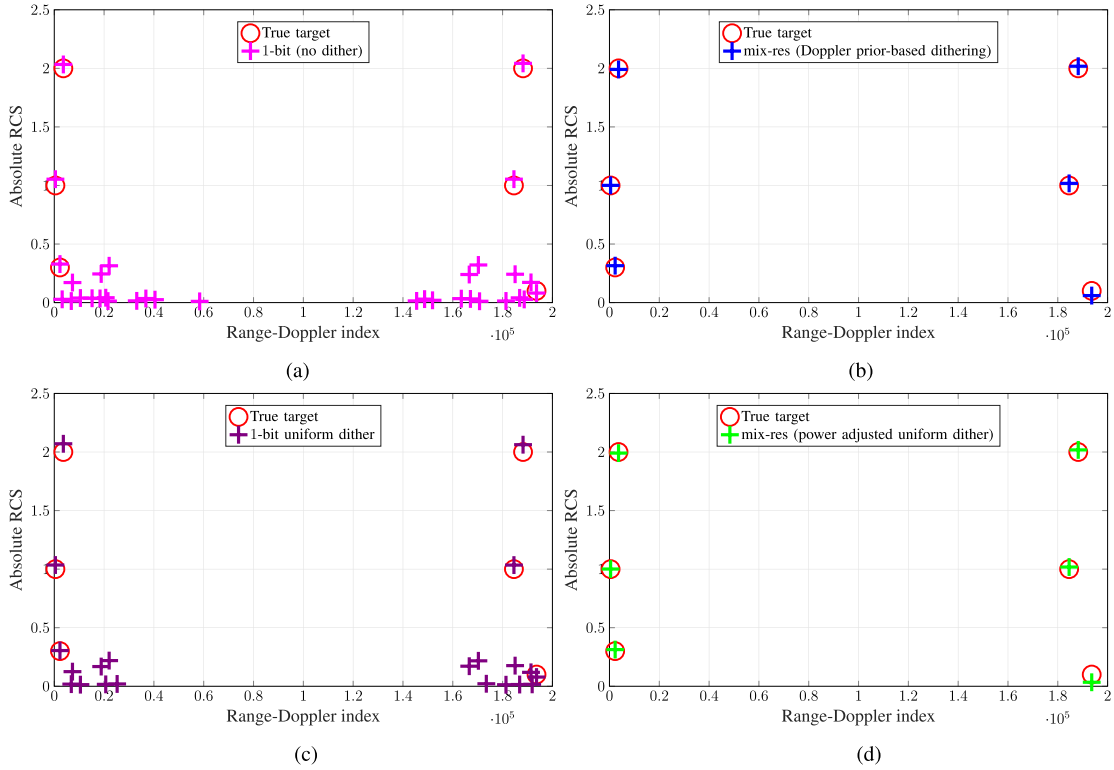

Fig. 17. Channel estimation results for the multilane highway scenario in Fig. 5 with different dithering signals and receiver designs. The proposed situation-aware dithering technique with a mixed-resolution ADC detects both high- and low-RCS targets, while a conventional one-bit system fails in detecting the low-RCS targets. (a) Conventional one-bit system. (b) Proposed mix-res system with Doppler prior-based dithering. (c) Conventional one-bit system with uniform dithering. (d) Mix-res system with power-adjusted uniform dithering.

bit system introduces significant false artifacts around the actual low-RCS targets due to its limited dynamic range. The use of uniformly distributed thresholds reduces these artifacts, but the issue of false alarms persists as seen in Fig. 17(c).

Fig. 17(b) and (d) showcases the channel estimation results obtained using the proposed mixed-resolution architecture with the Doppler-prior-based thresholds and power-adjusted uniformly distributed thresholds, respectively. The results clearly highlight the robustness of the mixed-resolution system. Our Doppler-prior-based dithering not only accurately estimates the weak targets but also minimizes false alarms significantly, even in the presence of strong reflections from high-RCS targets. In contrast, while the power-adjusted uniformly distributed thresholds show improvement over conventional one-bit systems, their performance deteriorates as the grid size decreases, consistent with earlier observations.

The proposed dither signal adapts to the radar channel realization by exploiting the high-resolution measurements. This adaptation ensures suppression of dominant target reflections, unmasking weaker targets such as the cyclist with higher accuracy. Furthermore, our dither signal leverages the Doppler prior by assigning Doppler priors to different lanes based on the range estimates from matched filtering. We observe that our method distinguishes closely spaced targets with overlapping Doppler shifts, such as the two trucks in lane-3, moving at 105 and 120 km/h. By ADC resolution adaptation and situation-aware dithering, our mixed-resolution system provides superior channel estimates from fewer measurements than conventional systems.

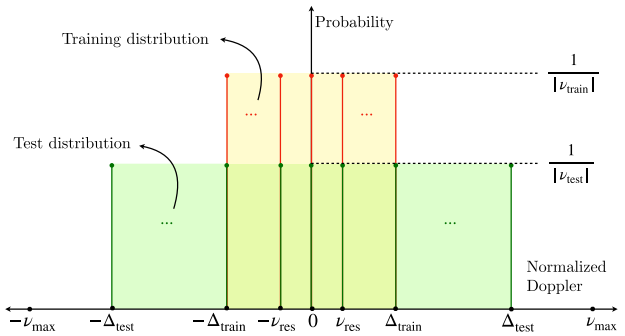

Fig. 18. Visual representation of training and test distributions for Doppler mismatch analysis.

D. Impact of Doppler Prior Mismatch

Our situation-aware dithering technique assumes perfect knowledge of the Doppler prior. In this section, we study how a mismatch in this prior impacts estimating the RCS of weak targets with our method. In our study, we consider one high-RCS target with $|\gamma| = 1$ and one low-RCS target with $|\gamma| = 0.1$.

Our dither signal is constructed by assuming that the Doppler prior is a uniform probability mass function over $[-\Delta_{\text{train}}, \Delta_{\text{train}}]$ in steps of the Doppler resolution ν_{res}, i.e., over the set defined as $\boldsymbol{\nu}_{\text{train}} = \{-\Delta_{\text{train}} : \nu_{\text{res}} : \Delta_{\text{train}}\}$. We denote this discrete uniform distribution, shown in Fig. 18, as $\mathcal{U}\{\boldsymbol{\nu}_{\text{train}}\}$ and the corresponding probability as $1/|\boldsymbol{\nu}_{\text{train}}|$. We call $\mathcal{U}\{\boldsymbol{\nu}_{\text{train}}\}$ the training distribution as the dither signal is generated based on this prior.

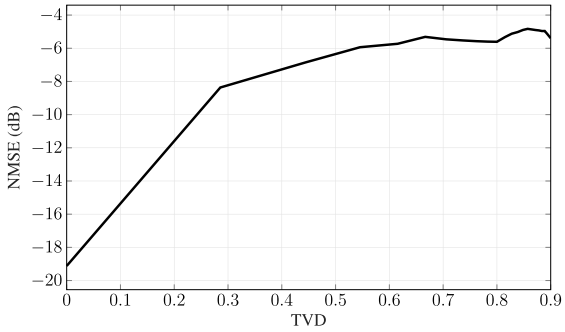

Fig. 19. Comparison of NMSE in the estimated RCS of the weak target in the presence of one dominant target for different TVD between the training and test Doppler distributions.

To study the robustness of our approach against Doppler prior mismatch, we consider a test distribution which also comprises Doppler values outside $\boldsymbol{\nu}_{\text{train}}$. For simplicity, we model the test distribution as a uniform prior over a wider Doppler ambiguity range, as shown in Fig. 18. This range is defined as $\boldsymbol{\nu}_{\text{test}} = \{-\Delta_{\text{test}} : \nu_{\text{res}} : \Delta_{\text{test}}\}$, where $\Delta_{\text{test}} \geq \Delta_{\text{train}}$, and the test distribution is $\mathcal{U}\{\boldsymbol{\nu}_{\text{test}}\}$ with a probability $1/|\boldsymbol{\nu}_{\text{test}}|$. To quantify the impact of prior mismatch on our method, we compute the average NMSE in the RCS estimate of low-RCS targets for each value of $\Delta_{\text{test}} \in \{\Delta_{\text{train}} : \nu_{\text{res}} : \nu_{\max}\}$ over multiple iterations. Each iteration employs a random realization of the dither signal generated from our training distribution. The mismatch between the training and testing Doppler distributions is quantified using the total variation distance (TVD) [39]. The TVD is 0 for identical distributions and is 1 for distributions supported on disjoint sets. For the distributions in Fig. 18, the TVD can be computed as

$$\text{TVD} = \frac{1}{2}\sum_{\nu \in \boldsymbol{S}} \left| \frac{\mathbf{1}_{\{\nu \in \boldsymbol{\nu}_{\text{train}}\}}}{|\boldsymbol{\nu}_{\text{train}}|} - \frac{\mathbf{1}_{\{\nu \in \boldsymbol{\nu}_{\text{test}}\}}}{|\boldsymbol{\nu}_{\text{test}}|} \right| \tag{24}$$

where $\boldsymbol{S} = \boldsymbol{\nu}_{\text{train}} \cup \boldsymbol{\nu}_{\text{test}}$, $\mathbf{1}_{\{\nu \in \boldsymbol{\nu}_{\text{train}}\}}$ is 1 if ν is in the training set, 0 otherwise, and similarly for $\mathbf{1}_{\{\nu \in \boldsymbol{\nu}_{\text{test}}\}}$. The TVD is higher for a large mismatch between the training and the test distributions.

Fig. 19 shows the NMSE for weak target RCS estimation and the TVD for $N = L = N_r = N_d = 50$, $\sigma^2/2 = 0.01$. Here, $\boldsymbol{\nu}_{\text{test}}$ includes 5 Doppler values centered around $\nu = 0$. We observe from Fig. 19 that the NMSE gets worse with an increasing TVD. Even under a prior mismatch of up to 0.3 TVD, our situation-aware dithering approach performs better than zero dithering. This follows from our observation that the NMSE with zero dithering (dotted blue curve in Fig. 14) is higher than the NMSE in Fig. 19 for a mismatched prior. Accounting for prior mismatch within the dithering method is an interesting research direction, which is beyond the scope of this article.

VII. Conclusion

We showed how ADC resolution adaptation, together with situation-aware dithering, can address the limited dynamic range problem in low-resolution radars. Our method sets a high resolution at the ADC in the first slow-time slot and a low resolution in the subsequent slots within a CPI. The high-resolution measurements acquired in the first slot, along with the Doppler statistics, are used to construct a dither signal to obtain low-resolution measurements. We also developed a radar channel estimation algorithm from the acquired mixed-resolution measurements. In addition, we presented a low-complexity implementation of our channel estimation technique using ZC transmit sequences. Through analysis and simulations, we demonstrated that our mixed-resolution architecture with situation-aware dithering not only achieves a higher probability of detection for low-RCS targets but also results in lower NMSE in channel estimates than benchmarks.

Appendix A
Derivation of $\mathcal{P}_{\text{FA}}$ and $\mathcal{P}_{\mathcal{D}}$ in (19) and (20)

Our derivation of $\mathcal{P}_{\text{FA}}$ and $\mathcal{P}_{\mathcal{D}}$ follows the analysis in [8], by incorporating an additional dither signal. Recall from Section IV that $f_1(\tilde{\mathbf{y}})$ and $f_0(\tilde{\mathbf{y}})$ are the pdfs under hypothesis $\mathcal{H}_1$ and $\mathcal{H}_0$, respectively, i.e.,

$$f_1\left(\tilde{\mathbf{y}}\left(\tilde{\boldsymbol{q}}\right)\right) = \prod_{m=1}^{2\,\text{NL}} \left[\mathcal{P}_{\tilde{\mathbf{y}}_m=1(\mathcal{H}_1)}\right]^{\frac{\tilde{\mathbf{y}}_m+1}{2}} \left[1-\mathcal{P}_{\tilde{\mathbf{y}}_m=1(\mathcal{H}_1)}\right]^{\frac{1-\tilde{\mathbf{y}}_m}{2}} \tag{25}$$

$$f_0\left(\tilde{\mathbf{y}}\left(\tilde{\boldsymbol{q}}\right)\right) = \prod_{m=1}^{2\,\text{NL}} \left[\mathcal{P}_{\tilde{\mathbf{y}}_m=1(\mathcal{H}_0)}\right]^{\frac{\tilde{\mathbf{y}}_m+1}{2}} \left[1-\mathcal{P}_{\tilde{\mathbf{y}}_m=1(\mathcal{H}_0)}\right]^{\frac{1-\tilde{\mathbf{y}}_m}{2}}. \tag{26}$$

Since the elements of the vector $\tilde{\mathbf{y}}$ are independent with each other and $\tilde{\boldsymbol{e}}$ is a vector with each element following an i.i.d. Gaussian distribution with zero mean and variance $\sigma^2/2$, we deduce:

$$\mathcal{P}_{\tilde{\mathbf{y}}_m=1(\mathcal{H}_1)} = 1-\Phi\left(\frac{-\sqrt{2}\tilde{\boldsymbol{\tau}}_{1,m}\left(\tilde{\boldsymbol{q}}_m\right)}{\sigma}\right)$$

$$\mathcal{P}_{\tilde{\mathbf{y}}_m=1(\mathcal{H}_0)} = 1-\Phi\left(\frac{-\sqrt{2}\tilde{\boldsymbol{\tau}}_{0,m}\left(\tilde{\boldsymbol{q}}_m\right)}{\sigma}\right).$$

Now, from (25) and (26), we obtain the one-bit logarithmic likelihood detector as

$$\ln \mathcal{T}\left(\tilde{\mathbf{y}}\left(\tilde{\boldsymbol{q}}\right)\right) = \tilde{\mathcal{T}}\left(\tilde{\mathbf{y}}\left(\tilde{\boldsymbol{q}}\right)\right) = \sum_{m=1}^{2NL} \tilde{\mathbf{y}}_m\left(\tilde{\boldsymbol{q}}_m\right)\boldsymbol{\rho}_m\left(\tilde{\boldsymbol{q}}_m\right) \underset{\mathcal{H}_0}{\overset{\mathcal{H}_1}{\gtrless}} \tilde{\xi}\left(\tilde{\boldsymbol{q}}\right).$$

Note that the one-bit outputs $\{\tilde{\mathbf{y}}_m(\tilde{\boldsymbol{q}})\}$ follow the Bernoulli distribution with probability $\mathcal{P} = 1-\Phi(-\sqrt{2}\tau_{i,m}(\tilde{\boldsymbol{q}})/\sigma)$ under $\mathcal{H}_i$. According to the central limit theorem [40], when NL is sufficiently large, the detector $\tilde{\mathcal{T}}(\tilde{\mathbf{y}}(\tilde{\boldsymbol{q}}))$ follows:

$$\tilde{\mathcal{T}}\left(\tilde{\mathbf{y}}\left(\tilde{\boldsymbol{q}}\right)\right) \overset{a}{\sim} \mathcal{N}\left(\mu_i\left(\tilde{\boldsymbol{q}}\right), \sigma_i^2\left(\tilde{\boldsymbol{q}}\right)\right), \text{ under } \mathcal{H}_i$$

where "a" denotes an asymptotic pdf. Finally, the expressions for $\mathcal{P}_{\text{FA}}(\tilde{\boldsymbol{q}})$ and $\mathcal{P}_{\mathcal{D}}(\tilde{\boldsymbol{q}})$ in (19) and (20), respectively, are obtained by evaluating

$$\mathcal{P}_{\mathcal{FA}}\left(\tilde{\boldsymbol{q}}\right) = \mathcal{P}\left\{\tilde{\mathcal{T}}\left(\tilde{\mathbf{y}}\left(\tilde{\boldsymbol{q}}\right)\right) \geq \tilde{\xi}\left(\tilde{\boldsymbol{q}}\right)|\mathcal{H}_0\right\}$$

$$\mathcal{P}_{\mathcal{D}}\left(\tilde{\boldsymbol{q}}\right) = \mathcal{P}\left\{\tilde{\mathcal{T}}\left(\tilde{\mathbf{y}}\left(\tilde{\boldsymbol{q}}\right)\right) \geq \tilde{\xi}\left(\tilde{\boldsymbol{q}}\right)|\mathcal{H}_1\right\}$$

which are written in terms of the complementary cdf of the standard normal distribution.

References

[1] S. M. Patole, M. Torlak, D. Wang, and M. Ali, "Automotive radars: A review of signal processing techniques," *IEEE Signal Process. Mag.*, vol. 34, no. 2, pp. 22–35, Mar. 2017.

[2] I. Bilik, O. Longman, S. Villeval, and J. Tabrikian, "The rise of radar for autonomous vehicles: Signal processing solutions and future research directions," *IEEE Signal Process. Mag.*, vol. 36, no. 5, pp. 20–31, Sep. 2019.

[3] C. Waldschmidt, J. Hasch, and W. Menzel, "Automotive radar—From first efforts to future systems," *IEEE J. Microw.*, vol. 1, no. 1, pp. 135–148, Jan. 2021.
[4] F. Roos, J. Bechter, C. Knill, B. Schweizer, and C. Waldschmidt, "Radar sensors for autonomous driving: Modulation schemes and interference mitigation," *IEEE Microw. Mag.*, vol. 20, no. 9, pp. 58–72, Sep. 2019.
[5] Y. Wu and J. Li, "The design of digital radar receivers," *IEEE Aerosp. Electron. Syst. Mag.*, vol. 13, no. 1, pp. 35–41, Jan. 1998.
[6] R. H. Walden, "Analog-to-digital converter survey and analysis," *IEEE J. Sel. Areas Commun.*, vol. 17, no. 4, pp. 539–550, Apr. 1999.
[7] K. U. Mazher, A. Mezghani, and R. W. Heath, "Low resolution millimeter wave radar: Bounds and performance," in *Proc. 52nd Asilomar Conf. Signals, Syst., Comput.*, Oct. 2018, pp. 554–558.
[8] Z. Cheng, Z. He, and B. Liao, "Target detection performance of collocated MIMO radar with one-bit ADCs," *IEEE Signal Process. Lett.*, vol. 26, no. 12, pp. 1832–1836, Dec. 2019.
[9] B. Jin, J. Zhu, Q. Wu, Y. Zhang, and Z. Xu, "One-bit LFMCW radar: Spectrum analysis and target detection," *IEEE Trans. Aerosp. Electron. Syst.*, vol. 56, no. 4, pp. 2732–2750, Aug. 2020.
[10] Y. Cheng, X. Shang, and F. Liu, "CRB analysis for mixed-ADC PMCW MIMO radar," in *Proc. CIE Int. Conf. Radar (Radar)*, Dec. 2021, pp. 1032–1037.
[11] M. Deng, Z. Cheng, L. Wu, B. Shankar, and Z. He, "One-bit ADCs/DACs based MIMO radar: Performance analysis and joint design," *IEEE Trans. Signal Process.*, vol. 70, pp. 2609–2624, 2022.
[12] Y.-H. Xiao, D. Ramírez, P. J. Schreier, C. Qian, and L. Huang, "One-bit target detection in collocated MIMO radar and performance degradation analysis," *IEEE Trans. Veh. Technol.*, vol. 71, no. 9, pp. 9363–9374, Sep. 2022.
[13] M. Deng, H. Wu, Z. Cheng, J. Wang, and Z. He, "Matched filtering performance analysis for massive MIMO radar with one-bit quantization," in *Proc. IEEE Radar Conf.*, May 2023, pp. 1–6.
[14] P. Stoica, X. Shang, and Y. Cheng, "The Cramér–Rao bound for signal parameter estimation from quantized data [lecture notes]," *IEEE Signal Process. Mag.*, vol. 39, no. 1, pp. 118–125, Jan. 2022.
[15] C.-Y. Wu, T. Zhang, J. Li, and T. F. Wong, "Parameter estimation in PMCW MIMO radar systems with few-bit quantized observations," *IEEE Trans. Signal Process.*, vol. 70, pp. 810–821, 2022.
[16] C. Gianelli, L. Xu, J. Li, and P. Stoica, "One-bit compressive sampling with time-varying thresholds for sparse parameter estimation," in *Proc. IEEE Sensor Array Multichannel Signal Process. Workshop (SAM)*, Jul. 2016, pp. 1–5.
[17] X. Shang, H. Zhu, and J. Li, "Range-Doppler imaging via one-bit PMCW radar," *Proc. IEEE Sens. Array Multichannel Signal Process. Workshop*, Jun. 2020, pp. 1–5.
[18] A. Ameri, A. Bose, J. Li, and M. Soltanalian, "One-bit radar processing with time-varying sampling thresholds," *IEEE Trans. Signal Process.*, vol. 67, no. 20, pp. 5297–5308, Oct. 2019.
[19] S. J. Zahabi, M. M. Naghsh, M. Modarres-Hashemi, and J. Li, "One-bit compressive radar sensing in the presence of clutter," *IEEE Trans. Aerosp. Electron. Syst.*, vol. 56, no. 1, pp. 167–185, Feb. 2020.
[20] T. Zhang, J. Ren, J. Li, L. H. Nguyen, and P. Stoica, "RFI mitigation for one-bit UWB radar systems," *IEEE Trans. Aerosp. Electron. Syst.*, vol. 58, no. 2, pp. 879–889, Apr. 2022.
[21] G. Zhang, W. Yi, M. Matthaiou, and P. K. Varshney, "Direct target localization with low-bit quantization in wireless sensor networks," *IEEE Trans. Signal Process.*, vol. 72, pp. 3059–3075, 2024.
[22] F. Xi, Y. Xiang, Z. Zhang, S. Chen, and A. Nehorai, "Joint angle and Doppler frequency estimation for MIMO radar with one-bit sampling: A maximum likelihood-based method," *IEEE Trans. Aerosp. Electron. Syst.*, vol. 56, no. 6, pp. 4734–4748, Dec. 2020.
[23] F. Foroozmehr, M. Modarres-Hashemi, and M. M. Naghsh, "Transmit code and receive filter design for PMCW radars in the presence of one-bit ADC," *IEEE Trans. Aerosp. Electron. Syst.*, vol. 58, no. 4, pp. 3078–3089, Aug. 2022.
[24] B. Wang, H. Li, and Z. Cheng, "Joint transceiver design for massive MIMO DFRC systems with one-bit DACs/ADCs," in *Proc. IEEE Globecom Workshops (GC Wkshps)*, Dec. 2023, pp. 649–654.
[25] F. Foroozmehr, M. Modarres-Hashemi, and M. M. Naghsh, "One-bit PMCW radar: Designing binary transmit code and receive filter via a worst-case approach," *IEEE Trans. Veh. Technol.*, vol. 73, no. 12, pp. 19774–19779, Dec. 2024.
[26] C.-Y. Wu, J. Li, and T. F. Wong, "Sparse parameter estimation for PMCW MIMO radar using few-bit ADCs," in *Proc. IEEE Int. Conf. Acoust., Speech Signal Process. (ICASSP)*, Jun. 2021, pp. 4415–4419.
[27] X. Shang, R. Lin, and Y. Cheng, "Mixed-ADC based PMCW MIMO radar angle-Doppler imaging," *IEEE Trans. Signal Process.*, vol. 72, pp. 883–895, 2024.
[28] M. Guo, K. Dai, X. Li, and Z. Zhao, "A bistatic MIMO radar system exploiting mixed-resolution quantization," *IEEE Trans. Veh. Technol.*, vol. 73, no. 12, pp. 19751–19755, Dec. 2024.
[29] M. Trakimas and S. R. Sonkusale, "An adaptive resolution asynchronous ADC architecture for data compression in energy constrained sensing applications," *IEEE Trans. Circuits Syst. I, Reg. Papers*, vol. 58, no. 5, pp. 921–934, May 2011.
[30] R. A. Stewart and E. Pfann, "Oversampling and sigma-delta strategies for data conversion," *Comput. Standards Interfaces*, vol. 21, no. 2, p. 97, Jun. 1999.
[31] S. O'Driscoll, K. V. Shenoy, and T. H. Meng, "Adaptive resolution ADC array for an implantable neural sensor," *IEEE Trans. Biomed. Circuits Syst.*, vol. 5, no. 2, pp. 120–130, Apr. 2011.
[32] A. Eamaz, K. V. Mishra, F. Yeganegi, and M. Soltanalian, "UNO: Unlimited sampling meets one-bit quantization," *IEEE Trans. Signal Process.*, vol. 72, pp. 997–1014, 2024.
[33] A. Bhandari, F. Krahmer, and R. Raskar, "On unlimited sampling and reconstruction," *IEEE Trans. Signal Process.*, vol. 69, pp. 3827–3839, 2021.
[34] J. Fang, F. Wang, Y. Shen, H. Li, and R. S. Blum, "Super-resolution compressed sensing for line spectral estimation: An iterative reweighted approach," *IEEE Trans. Signal Process.*, vol. 64, no. 18, pp. 4649–4662, Sep. 2016.
[35] R. Zhang, C. Li, J. Li, and G. Wang, "Range estimation and range-Doppler imaging using signed measurements in LFMCW radar," *IEEE Trans. Aerosp. Electron. Syst.*, vol. 55, no. 6, pp. 3531–3550, Dec. 2019.
[36] B. Zhao, L. Huang, and W. Bao, "One-bit SAR imaging based on single-frequency thresholds," *IEEE Trans. Geosci. Remote Sens.*, vol. 57, no. 9, pp. 7017–7032, Sep. 2019.
[37] J. Ren, T. Zhang, J. Li, and P. Stoica, "Sinusoidal parameter estimation from signed measurements via majorization–minimization based RELAX," *IEEE Trans. Signal Process.*, vol. 67, no. 8, pp. 2173–2186, Apr. 2019.
[38] C. Gianelli, L. Xu, J. Li, and P. Stoica, "One-bit compressive sampling with time-varying thresholds: Maximum likelihood and the Cramér-rao bound," in *Proc. 50th Asilomar Conf. Signals, Syst. Comput.*, Nov. 2016, pp. 399–403.
[39] T. M. Cover, *Elements of Information Theory*. Hoboken, NJ, USA: Wiley, 1999.
[40] S. M. Kay, *Fundamentals of Statistical Signal Processing: Estimation Theory*. Upper Saddle River, NJ, USA: Prentice-Hall, 1993.

Mohammed Aasim Shaikh (Graduate Student Member, IEEE) received the B.Tech. degree in electrical engineering from the IIT Gandhinagar, Gandhinagar, Gujarat, India, in 2021, and the M.Sc. degree in electrical and computer engineering (ECE) from the King Abdullah University of Science and Technology (KAUST), Thuwal, Saudi Arabia, in 2023. He is currently pursuing the Ph.D. degree with Delft Center for Systems and Control (DCSC), Delft University of Technology (TU Delft), Delft, The Netherlands, as part of the Signal Processing for Environmentally Aware Radar (SPEAR) Project in collaboration with NXP Semiconductors.

Geethu Joseph (Senior Member, IEEE), photograph and biography not available at the time of publication.

Ashish Pandharipande (Senior Member, IEEE), photograph and biography not available at the time of publication.

Nitin Jonathan Myers (Member, IEEE), photograph and biography not available at the time of publication.